Icarus 287 (2017) 87–102

Contents lists available at ScienceDirect

Icarus

journal homepage: www.elsevier.com/locate/icarus

Rarefied gas dynamic simulation of transfer and escape in the Pluto–Charon system

William A. Hoey[a,*], Seng Keat Yeoh[a], Laurence M. Trafton[b], David B. Goldstein[a], Philip L. Varghese[a]

[a] Department of Aerospace Engineering and Engineering Mechanics, University of Texas, Austin, TX 78712, United States
[b] Department of Astronomy, University of Texas, Austin, Texas 78712, United States

ARTICLE INFO

Article history:
Received 16 May 2016
Revised 12 October 2016
Accepted 5 December 2016
Available online 9 December 2016

Keywords:
Pluto
Pluto, atmosphere
Atmospheres, dynamics
Atmospheres, structure
Charon

ABSTRACT

We apply the direct simulation Monte Carlo rarefied gas dynamic technique to simulations of Pluto's rarefied upper atmosphere motivated by the need to better understand New Horizons (NH) data. We present a novel three-dimensional DSMC model of the atmosphere that spans from several hundred km below the exobase – where continuum flow transitions to the rarefied regime – to fully free-molecular flow hundreds of thousands of km from Pluto's center. We find molecular collisions in Pluto's upper atmosphere to be significant in shaping the flowfield, both by promoting flux from the plutonian exobase to Charon and by increasing the proportion of that flux generated on the exobase's anti-Charon hemisphere. Our model accounts for the gravitational fields of both Pluto and Charon, the centripetal and Coriolis forces due to the rotation of Pluto in our reference frame, and the presence of Charon as a temporary sink for impacting particles. Using this model, we analyze the escape processes of N_2 and CH_4 from Pluto across different solar heating conditions, and evaluate the three-dimensional structure of the upper plutonian atmosphere, including gas transfer to and deposition on Charon.

We find results consistent with the NH-determined escape rate, upper atmospheric temperature, and lack of a detectable Charon atmosphere. Gas-transfer structures are noted in a binary atmospheric configuration, including preferential deposition of material from Pluto's escaping atmosphere onto Charon's leading hemisphere that peaks at 315° E on the equator. As the moon gravitationally focuses incident flow, a high density structure forms in its wake. If molecules are permitted to escape from Charon in diffuse reflections from its surface, a returning flux forms to Pluto's exobase, preferentially directed toward its trailing hemisphere. Charon is capable of supporting a thin atmosphere at column densities as high as 1.5×10^{17} m^{-2} in simulations with a plutonian exobase condition similar to the NH encounter. Results computed from a fit to the NH encounter exobase (Gladstone et al., 2016) predict a system escape rate of 7×10^{25} CH_4 s^{-1} in close agreement with those reported by NH (Bagenal et al., 2016; Gladstone et al., 2016), and a net depositional flux to Charon of 2×10^{24} s^{-1}, of which ~98% is methane.

1. Introduction

The atmosphere of Pluto is supported by the vapor pressure of volatile ices, primarily N_2, with minor contributions from CH_4 and CO (Gladstone et al., 2016). Of these, N_2 dominates both in the ice phase (Owen et al., 1993) and in the lower atmosphere to 1800 km, although toward the exobase the abundance of minor species increases and CH_4 composes the majority of escaping flow (Gladstone et al., 2016). The volatile ices have a non-uniform distribution over Pluto and the ice mixture percentages, composition, and grain size also vary over the globe (Olkin et al., 2007; Protopapa et al., 2008; Grundy et al., 2014). Owing to a lower vapor pressure than for N_2, the atmospheric mixing ratio of CH_4 was projected to be on the order of 10^{-3} (O[10^{-3}]) prior to the New Horizons encounter (Young et al., 1997; Lellouch et al., 2015). The New Horizons methane atmospheric mixing ratio of ~0.25% was somewhat lower than the anticipated value of ~0.44% (Stern et al., 2015; Lellouch et al., 2015). However, NH found the concentration of methane at Pluto's exobase to be as high as ~42%, which suggests that methane, not nitrogen, composes the bulk of material transferred from the plutonian atmosphere to Charon and escaping the system. The hydrocarbons C_2H_2 and C_2H_4 have also been detected with atmospheric mixing ratios of $\sim 3 \times 10^{-6}$ and $\sim 1 \times 10^{-6}$ respectively (Stern et al., 2015).

* Corresponding author.
E-mail address: whoey@utexas.edu (W.A. Hoey).

http://dx.doi.org/10.1016/j.icarus.2016.12.010

The atmosphere of Pluto is complex and time-variable, as the plutonian surface experiences large changes in insolation during its orbit. Dramatic seasonal atmospheric changes were predicted beginning in the early 1980s (Stern, 1981; Trafton and Stern, 1983), driven by the sensitivity of vapor pressure to temperature, the large variation in Pluto's heliocentric distance (29.5–49.6 AU), and the high axial obliquity (120°) of the orbit of Pluto. Such changes are supported by several stellar occultation observations. Between observations in 1988 and 2002 the atmospheric pressure of Pluto was found to increase by a factor of two (Elliot et al., 1989; Hubbard et al., 1988; Millis et al., 1993; Pasachoff et al., 2005; Sicardy et al., 2003; Yelle and Elliot, 1997). Subsequent observations indicated that pressure continued to increase until leveling off after 2007, and has not since collapsed (Elliot et al., 2007; Zalucha et al., 2011; Olkin et al., 2014,2015). However, the upper atmospheric thermal structure remained largely the same throughout (Elliot et al., 2007; Person et al., 2008; Young et al., 2008). The New Horizons (NH) occultation experiment found a somewhat lower surface pressure (~10–11 microbars) than anticipated by extrapolating the ground-based stellar occultation results to the surface (Gladstone et al., 2016).

Pluto's atmosphere undergoes escape in a process that was once thought to be slow and hydrodynamic (McNutt, 1989; Yelle, 1997; Trafton et al., 1997; Krasnopolsky, 1999; Tian and Toon, 2005; Strobel, 2008), but that has since been demonstrated to occur on a molecule-by-molecule basis (Tucker et al., 2012, Erwin et al., 2013). A key finding of NH was that Pluto's upper atmospheric temperature of ~70 K was significantly colder than expected (Gladstone et al., 2016). Upper atmosphere occultation opacity indicated a dearth of nitrogen that could be reasonably fit by such a cold temperature. These results suggest there is an as-yet-unidentified radiative cooling mechanism, perhaps associated with C_2H_2 or HCN. This low upper atmospheric temperature reinforces the understanding of plutonian atmospheric escape as a process by which individual molecules at the tail end of the thermal velocity distribution at the exobase obtain sufficient upwardly-directed energy to escape in a Jeans process (Volkov et al., 2011), rather than via the slow hydrodynamic process that had informed models of the Pluto–Charon system prior to Tucker et al. (2012).

Moreover, the expected N_2 escape rate is reduced from pre-encounter predictions by four orders of magnitude, to $10^{23}\,s^{-1}$: such a low rate would be consistent with a much-reduced altitude of atmospheric interaction with the solar wind and an undetectably thin atmosphere at Charon. The exobase parameters referenced in this work as NH observations are the results of a model constrained by the LOS density measurements of Gladstone et al. (2016), which extend to 1500 km above Pluto.

1.1. Review of plutonian upper atmospheric models

Different regions on the surface of Pluto receive different amounts of insolation; this leads to a net sublimation-driven flow of volatile ices towards regions of lower insolation, forming 'sublimation winds'. This transfer of volatiles through the atmosphere is accompanied by a transfer of latent heat that effectively redistributes the absorbed solar heat to the entire exposed volatile surface, causing the volatile ice to be nearly isothermal (Trafton and Stern, 1983) though the composition of the volatile ice varies across the globe (Spencer et al., 1997; Protopapa et al., 2008; Grundy et al., 2014). To achieve a near-isothermal ice surface, the mass of the atmosphere must be large enough for it to be globally near hydrostatic equilibrium. In this case, the sublimation winds must everywhere be subsonic (Trafton and Stern, 1983; Ingersoll, 1990; Trafton, 1990; Trafton et al., 1997).

A significant fraction of the surface of Pluto is not volatile, so its temperature is regulated only by a balance between insolation and advection. However, the vapor pressure at the ice temperature governs the atmospheric pressure around the globe, including in regions lacking volatile ice. While the atmosphere breaks spherical symmetry by rotation, sublimation winds, and surface topography, all but recent upper atmospheric models of Pluto are essentially one-dimensional, providing the same vertical structure over the entire globe.

These 1-D models have been used to estimate the hydrodynamic escape rate of the atmosphere of Pluto at perihelion. Hunten and Watson (1982) pointed out that the escape of the atmosphere of Pluto, which was long thought to be hydrodynamic, is energy-throttled by adiabatic cooling of the expanding atmosphere, which is regulated by the downward conduction of solar EUV+UV heat absorbed in the thermosphere. Previous model-dependent hydrodynamic escape rates ranged from 10^{27} to $10^{28}\,s^{-1}$ (Hubbard et al., 1990; Krasnopolsky, 1999; McNutt, 1989; Trafton et al., 1997; Yelle, 1997).

McNutt (1989) used a self-consistent analytic approach to study the escape of CH_4 and CO and found the escape rate sensitive to solar EUV heating. Yelle (1997) accounted for solar EUV heating, thermal conduction and viscous mechanical dissipation and numerically solved the Navier–Stokes equations for the hydrodynamically escaping atmosphere of Pluto for N_2 and CO. Trafton et al. (1997) solved the hydrostatic escape equations for a CH_4 atmosphere and estimated an escape rate of $\sim 3.3 \times 10^{27}\,s^{-1}$. Krasnopolsky (1999) extended the analytic approach of McNutt (1989) to include several previously neglected terms, including the solar UV heating of the upper atmosphere of Pluto, which he argued was six times stronger than the solar EUV heating. Then, he applied his approach to the hydrodynamic escape of N_2 from Pluto, with CH_4 diffusing upward through it, and found substantial variations in the structure of the extended atmosphere of Pluto and the escape rate with solar cycle. He estimated the N_2 escape rate of $(2.0\text{–}2.6) \times 10^{27}\,s^{-1}$ at mean solar activity and varies by a factor of 3–4 over a solar cycle.

Tian and Toon (2005) solved the time-dependent hydrodynamic escape equations for a planetary atmosphere and applied them to the hydrodynamic escape of N_2 from Pluto, deriving a perihelion escape rate an order of magnitude higher than Krasnopolsky (1999). They argued that this discrepancy arose from the single-altitude heating approximation made by Krasnopolsky. Strobel (2008) solved the steady-state equations for hydrodynamic escape and accounted for the solar EUV heat absorbed by N_2, the near-IR and UV heat absorbed by CH_4 and the rotational cooling by CO as a function of solar activity. At the time of the NH flyby in July 2015, they predicted an N_2 escape rate of $\sim 2.2 \times 10^{27}\,s^{-1}$ and a peak thermospheric temperature of ~103 K at a radial distance of 1890 km.

1.2. Kinetic, rarefied gas dynamic simulation of the Pluto–Charon system

The calculations above were made based on the continuum assumption, which is valid only in the lower atmosphere. This assumption fails approaching the exobase, necessitating the use of a kinetic model of the upper atmosphere. Tucker et al. (2012) modeled the continuum region of the atmosphere with one-dimensional fluid equations and coupled this model to a direct simulation Monte Carlo (DSMC) kinetic model of the upper atmosphere to constrain the thermally-driven escape of N_2 from Pluto. They adopted the temperature and density profiles of Strobel (2008) and considered two solar heating conditions, obtaining escape rates of $\sim 4.8 \times 10^{25}\,s^{-1}$ and $\sim 1.2 \times 10^{27}\,s^{-1}$, respectively. These rates are comparable to the Jeans escape rates for the same conditions. They concluded that the thermally-driven escape from Pluto is therefore similar in nature to Jeans exospheric escape, and must be treated on a molecule-by-molecule basis to account for its non-Maxwellian molecular speed distribution.

Charon is located ~19,600 km from Pluto (~17 Pluto radii) and its Hill sphere extends as close to Pluto as ~12,700 km. Its presence contributes to the three-dimensionality of Pluto's atmosphere, as Charon gravitationally perturbs flow from Pluto's exobase. The three-dimensional, free-molecular simulations of Tucker et al. (2015) demonstrated several significant binary atmospheric phenomena, including the influence of Charon on the morphology of the system's density field and the potential for Roche-like atmospheric transfer to, and the persistence of a thin atmosphere about, Charon itself. These simulations predicted that the atmosphere of Pluto would, at nominal solar heating conditions, deposit molecules on the surface of Charon at a rate of O[10^{25}] s^{-1}.

In this work, we present a DSMC model of the plutonian atmosphere from its exobase out to hundreds of thousands of km. While the lower, continuum atmosphere of Pluto is complex and three-dimensional in nature, we only consider the effects of Pluto's rotation and input particles into the simulation domain with the appropriate conditions at the lower boundary. In the future, we aim to use input conditions derived from a full three-dimensional simulation using a global climate model (GCM) of the lower atmosphere of Pluto. Our model accounts for both the gravitational fields of Pluto and Charon, the centrifugal and Coriolis forces due to the rotation of Pluto, and the presence of Charon as a sink for impacting particles.

Our DSMC model improves upon the simulations of Tucker et al. (2012, 2015) by representing collisions in our simulation over a three-dimensional domain including Charon that extends from the sub-exobase region of Pluto out to 32,000 km in radial distance, well past the transition to free-molecular flow. To prevent aphysical escape, a free-molecular region is appended to our domain that extends to 150,000 km, with a boundary that specularly reflects particles that have insufficient mechanical energies to escape the system at that distance. This reflection is energy-preserving, and accurate in the steady-state solution over the time-span of these simulations to the extent that the flow is nearly axisymmetric at the boundary surface. The one-dimensional simulations of Tucker et al. (2012) only consider collisions to 10,000 km and neglect Charon's influence on the flow entirely, while the three-dimensional simulations of Tucker et al. (2015) that include Charon neglect collisions above the exobase, employing instead an entirely free-molecular model that corrects for the effect of collisions in enhancing transfer and escape fluxes by increases in lower boundary temperature. We find that the consideration of collisions alters the flowfield, most notably by promoting flux to Charon by O[10%] and increasing the proportion of that flux generated on the anti-Charon hemisphere of Pluto's exobase between the Case A simulation presented in Section 3 and a trial, free-molecular solution. Furthermore, we markedly increase the resolution in computational particles compared to previous work, with values of f_{num} ranging from 3×10^{24} to 5×10^{25} in the cases presented in Sections 3 and 4, allowing us to obtain better statistics, reduce noise and improve spatial resolution in our results. We also employ a two-species model that includes methane, whereas Tucker et al. (2015) considered only escaping nitrogen.

Using this model, we analyze the transfer and escape processes of N_2 and CH_4 from the plutonian exobase, with boundary conditions at the exobase interface as functions of solar heating. We consider several heating conditions, focusing on a comprehensive, high-resolution simulation with an exobase equivalent to the unheated atmosphere computed in Tucker et al. (2012) and a case computed in response to the observed conditions at the New Horizons encounter. The minimum, medium, and maximum solar heating cases considered in Tucker et al. (2015) are addressed in Appendix C. In particular, we examine the processes of gas falling back through the lower boundary and of gas escaping the Pluto–Charon system, including calculated escape rates. We also investigate the deposition of gas over the surface of Charon, including the spatial distributions of the impacting particles. This helps us to ascertain whether Charon has an atmosphere, and how dense such an atmosphere might be. This is constrained by the New Horizons observation of no detectable atmosphere at Charon, bracketing the maximum possible extent of Charon's atmosphere to be roughly O[1 picobar] in pressure or O[10^{20} m^{-2}] in column density (Stern et al., 2015,2016; Gladstone et al., 2016). In addition, we use our model to investigate the three-dimensional fields of several gas properties, including density and temperature, around Pluto and Charon. This enables us to gain a better understanding of the mechanisms underlying the atmospheric escape process and the transfer of material between Pluto and Charon. As new NH data become further available, the current modeling work will provide a framework for future improvements, including coupling to a GCM model of the lower atmosphere for more accurate input conditions at the lower boundary and the inclusion of other gas species, such as CO.

In Section 2, we describe the DSMC model, including the assumptions made and the physics used. In Section 3, we present our results for and discuss the flowfield evolving from a pre-encounter unheated exobase while, in Section 4, we present and discuss a simulation of the Pluto–Charon system at the New Horizons encounter. In Section 5 we summarize our findings, give conclusions, and propose future work.

2. Methodology

2.1. DSMC method

DSMC uses a representative set of computational particles to model the movements and collisions of real molecules in dilute gas flows (Bird, 1994). Each computational particle represents a large number of real gas molecules, denoted as f_{num}, which is typically on the order of 10^{24}–10^{26}. A DSMC domain is decomposed into multiple cells in which particles move and collide. Only particles within the same cell can collide, and they do so in a probabilistic manner. Between collisions, particles translate in a ballistic manner under the influence of any force field present (e.g. gravity). The key assumption in DSMC is that the particle movement and collision phases can be decoupled over a time interval much shorter than the mean collision time, τ_{coll}. Consequently, the particle collision and movement phases are executed in sequence in DSMC over a timestep, Δt, chosen to be much smaller than τ_{coll}. Macroscopic flow properties (e.g. temperature and velocity) are obtained by averaging over the appropriate molecular properties in each cell.

DSMC has been shown to satisfy the collision integral in the Boltzmann equation (Nanbu, 1986) and solve the Boltzmann equation itself (Wagner, 1992). Therefore, it is valid over all flow regimes, from continuum to free-molecular. However, it is usually used to only model rarefied gas flows because it is prohibitively computationally expensive to model continuum flow using DSMC. DSMC is suitable for modeling the atmosphere of Pluto from well below the exobase region out to hundreds of thousands of km as the flow passes through multiple regimes, from moderately collisional in the exobase region to free-molecular far away. Moreover, the non-equilibrium nature of such flows can be captured by DSMC, which accounts for the different internal molecular energy modes (e.g. rotational and vibrational) and the energy exchange between them. As demonstrated by Beth et al. (2014), this sort of collisional kinetic model is necessary to generate particles that populate satellite orbits, which, in some cases, can compose a majority of those at sufficient distance above a planetary exobase. However, in the Pluto–Charon system and in these simulations, perturbations due to Charon prevent satellite particles from forming long-term stable orbits. Perturbations not represented in this work – for instance, those due to other Pluto-system moons, radiation pressure, and solar wind interaction – may also act to eliminate satellite particles.

2.2. DSMC implementation

We use a planetary DSMC code developed from the original procedure introduced by Bird (1994) that has been applied in simulations of the volcanic plumes and atmosphere of Io (McDoniel et al., 2015; Moore et al., 2009; Walker et al., 2010, 2012; Zhang et al., 2003, 2004), the south polar two-phase plume of Enceladus (Yeoh et al., 2015), comet impacts on the moon (Prem et al., 2015; Stewart et al., 2011), and the plume impingement of landing rockets on the lunar surface and the resulting dispersal of dust (Morris et al., 2015). While the DSMC code contains many features, we only highlight those relevant to the current problem in this section.

In our current simulations, we consider a mixture of CH_4 and N_2. The molecular model used is the variable hard sphere (VHS) model with the appropriate parameters for both species (Bird, 1994). We track the internal energy states of the gas molecules, notably the rotational and vibrational states, though the vibrational modes are hardly excited at the low temperatures of Pluto ($\leq$100 K). Energy exchanges occur between the translational and the internal modes as well as among the internal modes through collisions via the statistical Larsen–Borgnakke exchange model (Borgnakke and Larsen, 1975; Bird, 1994).

Our calculations are performed in a non-inertial reference frame that is fixed to Pluto and rotates with it, with an origin located at the center of Pluto. Therefore, between collisions, the computational particles travel along ballistic trajectories under the influence of not only the gravitational fields of Pluto and Charon but also the Coriolis and centrifugal forces arising from rotation in this frame. In our simulations, the equation of motion of a particle between collisions is given by:

$$\ddot{\boldsymbol{r}}_{\boldsymbol{part}} = \boldsymbol{g_P} + \boldsymbol{g_C} - 2(\boldsymbol{\omega_P} \times \dot{\boldsymbol{r}}_{\boldsymbol{part}}) - \boldsymbol{\omega_P} \times (\boldsymbol{\omega_P} \times \boldsymbol{r}_{\boldsymbol{part}}) \tag{1}$$

where $\boldsymbol{r}_{\boldsymbol{part}}$ is the position vector of the particle. The superscript dot notation indicates differentiation with respect to time. The first two terms on the right hand side, $\boldsymbol{g_P}$ and $\boldsymbol{g_C}$, are the variable gravitational accelerations due to Pluto and Charon respectively, which are proportional to the inverse of the square of the distance of the particle from the centers of the respective parent bodies. The third and fourth terms are the Coriolis and centrifugal accelerations respectively, where $\boldsymbol{\omega_P}$ is the rotational velocity of Pluto.

The barycenter of the Pluto–Charon system is located *outside* either body at ~2042 km from the center of Pluto along the line connecting the centers of the two bodies. Pluto and Charon are mutually tidally locked to one another, thus the rotational and orbital periods of Charon and the rotational period of Pluto are all equal. The Pluto–Charon system used in our simulations is shown in Fig. A.1., where we have made the following simplifying approximations:

(i) The orbital plane of Charon coincides with the equatorial plane of Pluto.
(ii) Charon executes a perfectly circular orbit around Pluto.
(iii) The axes of rotation of both Pluto and Charon are perpendicular to the orbital plane of Charon (and thus also the equatorial plane of Pluto).

These approximations are corroborated in the initial New Horizons report, which finds Charon's orbital inclination with respect to the equatorial plane of Pluto to be 0.0° while its orbital eccentricity is ~0.00005 (Stern et al. 2015). The important geometric parameters of the Pluto–Charon system used in our simulations are summarized in Table A.1., and compared to the values recorded by NH and those employed in simulations in the literature. Pluto exhibits an axial tilt of ~120° relative to the ecliptic, but these simulations do not incorporate solar dependence in heating models or exobase boundary conditions.

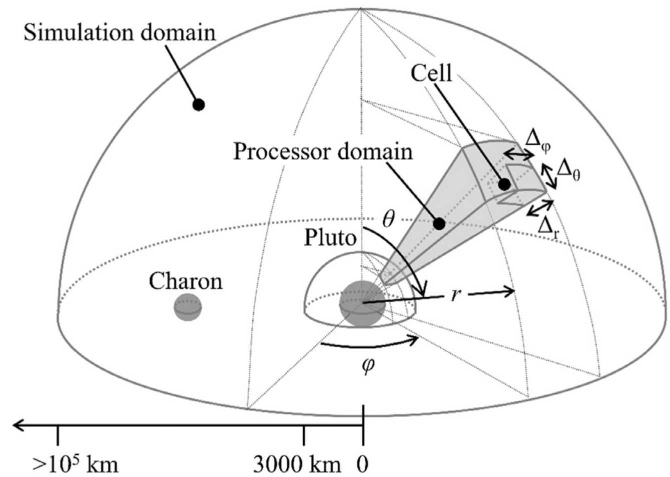

Fig. 1. Shape and extent of simulation domain, processor domain and cell used in this work. Note that drawing is not to scale.

The positions and velocities of the particles are obtained by integrating Eq. (1) using an 8th-order adaptively-stepped error-controlled Runge–Kutta Prince–Dormand scheme. The Lagrange point between Pluto and Charon (typically labeled L1) plays an important role in material transfer and the structure of the number density field. This Lagrange point is unstable, thus a particle placed there will ultimately depart from equilibrium due to any slight perturbation, including the round-off errors introduced by numerical integration. We performed a study to compare this integration scheme with a 2nd-order predictor-corrector scheme employed in our prior DSMC applications and in Tucker et al. (2015), more details on which can be found in Appendix B.

2.3. Simulation parameters

DSMC requires that the cell size and Δt be smaller than the scale length, L, of the microscopic flow gradients and τ_{coll} respectively (Bird, 1994). For our purposes, L is chosen to be based on the gradients of the gas density, ρ: $L \triangleq \rho/|\nabla\rho|$ (Bird, 1994). Since macroscopic flow gradients are not expected over length scales shorter than the local mean free path of the gas, λ, i.e. $\lambda < L$, the cell size requirement is satisfied if the cell size is smaller than λ. Our DSMC code uses a *spherical* coordinate grid that allows for non-uniform cell size distribution in each of the radial (r), zenith (θ) and azimuthal (φ) directions, as shown in Fig. 1. We have chosen a cell size distribution in each direction such that the cell sizes are smaller than λ everywhere in the simulation domain. We have also chosen Δt to be smaller than τ_{coll} everywhere; at the exobase, the most restrictive times between collisions are O[10^2] s. More details on the various simulation parameters used can be found in Appendix A.

Based on our simplifying approximations made to the system, we expect symmetry across the equatorial plane of Pluto and thus only simulate the region north of the equatorial plane. Our simulation domain is hemispherical in shape and centered on Pluto, extending in the radial direction from the exobase to $>1.5\times10^5$ km (~$2.5R_P$ to $>126.5R_P$) from the center of Pluto, as shown in Fig. 1. Within Pluto's gravitational predominance, a Knudsen number can be defined based on the atmospheric scale height: $Kn_H \triangleq \lambda/H_P$, where H_P is the atmospheric scale height of

Pluto, defined as: $H_P \triangleq (k_b T) / (m_i g)$, where k_b is the Boltzmann constant, T is the local temperature of the gas, m_i is the mass of an individual molecule, and $g(r)$ is the local gravity. Each species has a separate characteristic scale height, dependent on its mass; at equivalent density and altitude, methane's lower mass relative to nitrogen will facilitate its preferential escape. While the exobase by definition occurs at the $Kn_H = 1$ interface, the simulations described herein draw their lower boundary conditions from work which employs slightly different values for the system geometry, as detailed in Table A.1. (Tucker et al., 2015; Stern et al., 2015). We opt to preserve reported number densities, temperatures, and exobase locations as ratios of R_P such that, at the lower boundary, simulation Kn_H are between 0.1 and 1.0. As upper atmospheric flow becomes more rarefied and transitions to free-molecular with radial distance from the plutonian exobase, Kn_H approaches infinity.

With the time-invariant flux of particles into our domain across the lower boundary (exospheric) surface, a steady state is expected to develop for atmospheric and escaping flow in our rotating reference frame. We run our simulation until this steady state is achieved within the domain, which typically takes on the order of ~8×10^6 s, or about fifteen system orbits. Our simulation has evolved to equilibrium when the following quantities reach their respective steady values:

(i) Total number of particles in the simulation domain
(ii) Particle flux across the *lower* boundary (out of domain)
(iii) Particle flux across the *upper* boundary
(iv) Particle flux onto the surface of Charon

Each of these quantities reaches their steady values at a different rate, and we begin to sample the flow field after steady-state is achieved. To reduce the statistical noise present in the samples, we perform long term time-averaging.

2.4. Computational methodology

Particles are introduced into the simulation domain through the lower boundary as a Maxwellian flux, with the number density and temperature along that boundary specified according to the solar heating conditions considered. For a particular cell along the lower boundary, the average number of computational particles generated per timestep, Δt, is given by:

$$N_{create} = \sqrt{\frac{k_b T_{cell}}{2\pi m_i}} \left[\frac{n_{cell} A_{cell} \Delta t}{f_{num}} \right] \tag{2}$$

where T_{cell}, n_{cell} and A_{cell} are the temperature, number density and surface area of the cell at the lower boundary, respectively. The particles are placed across the cell surface according to a uniform random distribution while their velocities are randomly drawn from a half-range Maxwellian distribution corresponding to T_{cell}. In the current work, we assume uniform conditions across the entire lower boundary. The values of number density and temperature used can be found in Appendix A. Global uniformity is a reasonable approximation, as corroborated by the New Horizons observation of a nearly isotropic exobase (Stern et al., 2015; Gladstone et al., 2016). In the future, we aim to obtain the lower boundary conditions derived from a three-dimensional simulation using a GCM of the lower atmosphere of Pluto.

Unless noted otherwise, any particle impacting Charon in this work is removed from the simulation domain: thus, Charon acts as a sink for particles. For each such particle, the time and spatial coordinates of exobase generation and impact on Charon are stored, in addition to particle species. This information is used to analyze the nature of deposition onto Charon for the limiting case in which all particles that impact, stick. It is also used to generate supplementary simulations in which these same particles instead equilibrate with the surface and diffusely reflect from Charon on impact, with their resultant velocities drawn from a half-range Maxwellian distribution at the imposed surface temperature, and continue to diffusely reflect until they achieve escape velocity. In the highly-rarefied (nearly free-molecular) flow regime about Charon, it is permissible to superpose the resultant number density fields to compare the opposing extremes of total sticking and total diffuse-reflection at Charon. As more data become available, e.g. detailed maps of Charon's surface temperature, frost coverage, and composition, we will implement more complex and realistic boundary conditions. While the Charon surface temperature employed in the present work is taken to be an isotropic 53 K, with a global map of surface temperature, we could implement a sticking boundary condition where only a fraction of impacting particles stick to the isotropic surface (Tucker et al. employ a simple linear distribution of temperature with latitude as nitrogen interacts with Charon in their 2015 work). If frost coverage and properties are also known, we can enforce a residence time for the sticking particles, introducing transient variability as particles stay stuck to the surface for a finite period of time and are then released back into the flow. These mechanisms are comparable to those developed in our codebase for simulation of adsorbing and desorbing sulfur dioxide in the comprehensive Ionian atmospheric simulations of Walker et al. (2012). The precise nature of particle interaction with the Charon surface is a critical boundary condition for study of local atmospheric dynamics and the propagation of transferred material to regions of the Charon surface, as to the cold-traps in polar regions that are eventually photolytically processed into tholins (Grundy et al., 2016). However, we do not anticipate the boundary conditions implemented on Charon to have a significant effect on vacuum escape rates or overall flowfield structure because only a small proportion of the escaping flow ends up impacting Charon (approximately 3.3–3.6%, see Tables 2 and C.2.).

The simulations are computed in parallel on multiple processors distributed along the azimuthal and zenith coordinates. An example of a simulation domain is shown in Fig. 1. In this work, a single run is typically performed on 240 processors over several dozen hours, or O[10^3–10^4] CPU-hours. We have distributed the processors in a non-uniform grid in zenith concentrated about the equatorial plane such that the total number of computational particles per processor does not vary significantly. In a typical simulation, the total number of computational particles per processor is O[10^6], with O[10^8] occupying the complete domain at any one time, and as many as O[10^{11}] distinct particles generated over the course of a run to steady-state. Pseudo-random number generation with the Mersenne twister SFMT19937 algorithm is employed to ensure valid statistics, and is vectorized for speed.

In our simulations, we have maintained O[10^2] particles per cell near the lower boundary with values of f_{num} varying across simulations from 10^{24} to 10^{26}. Adequate resolution in particle count is especially important near the lower boundary where the flow is densest and most collisional, as two or more computational particles are required in a cell for collisions to actually occur. While cells expand in volume with radial distance from the exobase, it is not necessary to maintain correspondingly high particle counts per cell as the flow becomes increasingly less collisional. Multiple cubic mean-free-paths are resolved everywhere throughout the flow.

2.5. Pre- and Post-encounter cases

In the following sections, we examine two cases, distinct in exobase boundary conditions, to illustrate the effect of upper atmospheric temperature and methane fraction on the overall atmospheric structure. Case A represents a cool, not cold, atmosphere case in which lower boundary conditions are drawn from one-dimensional hybrid fluid-kinetic simulations of the atmosphere

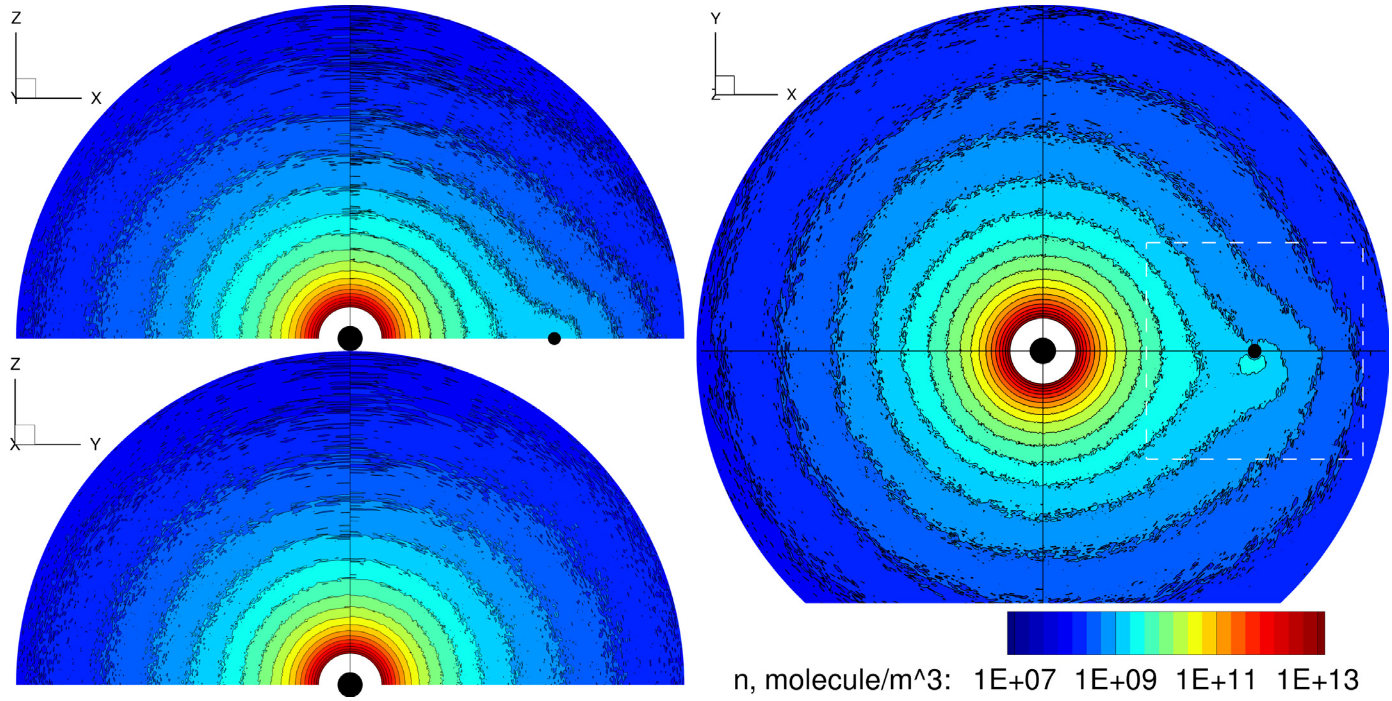

Fig. 2. A three panel view shows orthogonal cut-planes in contours of total number density. Pluto and Charon are marked in black, and Pluto's collisional atmosphere in white. Both bodies are rotating counterclockwise when viewed down the polar Z axis (at right), and are likewise revolving CCW about the barycenter. Note the distortion of the density field due to Charon's gravity, and the evident transfer of escaping atmosphere to a high-density region at Charon's trailing hemisphere. The dashed white square is the region about Charon, 20,000 km on edge, considered in detail in Figs. 4 and 5.

below the exobase by Tucker et al. (2012) without solar heating, for which converged values of temperature and number density are reported at R = 2,836 km. This condition was employed isotropically in preliminary three-dimensional simulations of the near-exobase region, not addressed herein, from which the converged Case A boundary condition at R= 3,000 km and Kn_H ~0.4 is drawn. In contrast, Case B matches its exobase directly to the lower boundary conditions determined by the ALICE and REX instruments on NH at two locations (during ingress and egress) as reported by Gladstone et al. (2016). Therefore, this result represents the nature of the three-dimensional atmospheric structure at the time of the NH encounter. In Appendix C, we pursue three other cases for direct comparison to and in extension of the previous work of Tucker et al. (2015), corresponding to various levels of applied solar heating in the lower continuum atmosphere. Those simulated atmospheres are more expansive than that observed by NH, with warmer exobases and higher nitrogen fractions, but could correspond to hypothesized instances of high rates of nitrogen escape in the past (Gladstone et al., 2016).

3. An unheated exobase

We first consider Case A, an hemispherically-symmetric atmosphere generated just below the exobase at 1,815 km above Pluto (R = 3,000 km) with total number density 1.34×10^{13} m^{-3}, temperature 85.5 K, f_{num} 3×10^{24}, and composition 99.56% N_2 and 0.44% CH_4 by mole as consistent with an evenly-mixed methane fraction through the upper atmosphere (Young et al., 1997; Lellouch et al., 2015). Results are presented for a steady-state simulation equilibrated over 16 million s (29 diurnal cycles) performed on the TACC Stampede supercomputer cluster on 240 processors at approximately 50,000 CPU hour expense. The number density field presented in Fig. 2 captures the evolved flowfield in a reference frame fixed to Pluto and in which Charon, due to the system's mutual tidal lock, remains stationary. The limit of the domain shown in this figure is 32,000 km from Pluto's center, but an appended free-molecular domain (not pictured) extends to 150,000 km.

With radial distance from the isotropic exobase, the density field distorts toward Charon along the Pluto–Charon axis, ultimately creating a bridging structure that arcs through the L1 Lagrange point and toward Charon's trailing (wakeward) hemisphere, while a corresponding and diffuse return flux passes material from Charon back to the wakeward side of Pluto. The density increase about Charon occurs primarily near the equatorial plane in this case for which all particles that strike Charon stick to its surface. Fig. 2 demonstrates these novel structures in the number density field on a set of three mutually orthogonal cut-planes intersecting at Pluto's center. The Case A exobase is detailed in Table 1, and related to the New Horizons observation and the minimum solar heating exobase calculated pre-encounter by Tucker et al. (2015). The variance in exobase position between Case A and the unheated, one-dimensional fluid-kinetic result reported by Tucker et al. (2012) stems from use of a different collision cross section in the VHS molecular model of our DSMC approach and minor updates to Pluto system values. Number densities and temperatures in the isotropic near-exobase region of the Case A flowfield otherwise match closely with the 2012 result.

The key differences between Case A and the NH encounter are in temperature and methane fraction: New Horizons encountered a surprisingly cold exobase, with fully ~42% methane by molar fraction. Total exobase number density for the unheated Case A lower boundary falls within the observed bounds, and the exobase position within 0.1 R_P. While a cold exobase slows escape to vacuum, as relatively few particles cross the exobase with energies sufficient to depart Pluto, this effect is counteracted by methane's low mass and correspondingly high scale height: relative to nitrogen, methane preferentially escapes. The non-dimensional Jeans parameter captures this behavior, and is used to calculate unperturbed Jeans escape rates: Jeans theory predicts that the New Horizons exobase will have escape rates 2–3 times higher than Case A, with methane composing over 99% of escaping material.

Table 1
The Case A exobase parameters compared against the conditions observed by New Horizons, the nominal solar-heating case applied in the Tucker et al. (2015) pre-encounter prediction, and the one-dimensional unheated case considered in Tucker et al. (2012).

Exobase	Radius [R_P/km]	T [K]	Density [m^{-3}]	N_2 [m^{-3}]	CH_4 [m^{-3}]	λ_J, N_2	λ_J,CH_4
Case A Result	2.59 R_P/3070	85.5	9.10×10^{12}	9.04×10^{12}	5.46×10^{10}	11.2	6.4
New Horizons	2.36 R_P/2800	70.0	7–12 $\times 10^{12}$	4–7 $\times 10^{12}$	3–5 $\times 10^{12}$	14.1	8.1
Tucker et al. (2015)	6.84 R_P/8105	79.0	5.0×10^{11}	5.0×10^{11}		4.8	
Tucker et al. (2012)	3.29 R_P/3900	85.0	1.7×10^{12}	1.7×10^{12}		8.8	

Table 2
Rates of flux into and out of the domain at the exobase boundary, to vacuum (the system escape rate), and to Charon for each species in the DSMC Case A calculation are compared to the NH encounter and the nominal and unheated cases in the literature.

Fluxes, all [s^{-1}].	Boundary [In]	Boundary [Out]	Escape rate	To Charon: N_2	To Charon: CH_4
Case A Result	9.64×10^{28}	9.63×10^{28}	3.6–4.2 $\times 10^{25}$	1.4–1.5 $\times 10^{24}$	1.5–1.6 $\times 10^{23}$
New Horizons			5–6 $\times 10^{25}$		
Tucker et al. (2015)	2.5×10^{28}	2.3×10^{28}	2.2×10^{27}	5.7×10^{25}	
Tucker et al. (2012)			4.8×10^{25}		

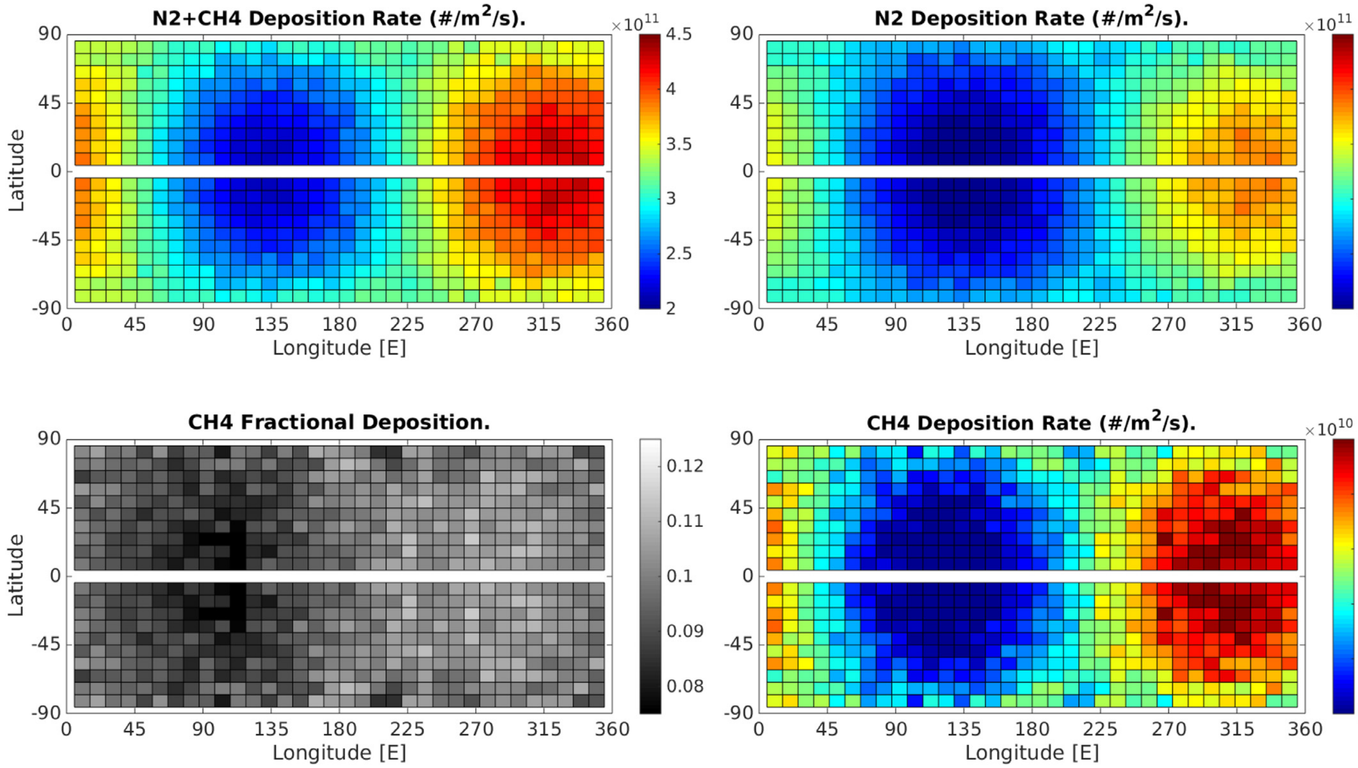

Fig. 3. In the DSMC simulations shown here and in Fig. 2, particles that strike Charon stick and are stored. Depositional rates onto Charon's surface for Case A (a no-heat exobase) are shown alongside the fraction of methane in the incident material, of order ∼10%. Data mirrored over the equator for clarity.

At steady-state, the DSMC simulation yields rates of molecule flux into and out of the domain, including rates of vacuum escape and flux to Charon by species. Table 2 reports these rates in comparison with relevant values from the NH observation and prior simulations. The Tucker et al. (2015) pre-encounter prediction represents the result of a three-dimensional free-molecular simulation in a comparable domain to the DSMC, but with a lower-atmospheric solar heating model inconsistent with Case A. The Tucker et al. (2012) result noted is consistent with the Case A no-heating condition, but calculated in a one-dimensional domain. The steady-state Case A vacuum escape rate is shown to be in good agreement with the NH observation, underpredicting the encounter value by just ∼30%.

Particles incident on Charon are recorded, and maps of deposition by species are shown in Fig. 3. Total deposition onto Charon is slightly in excess of 10% methane by mole for the Case A lower boundary conditions, a significant increase over the generation fraction of 0.44%. Both methane and nitrogen are observed to deposit preferentially onto Charon's leading hemisphere with peak flux at about 315° E (45° W) longitude, although the difference between the global minimum (at 135° E) and maximum depositional rates is only a factor of two. This depositional pattern represents only the *initial* impact of particles onto Charon. The result that Charon's leading face experiences peak deposition while a high density structure forms in Charon's wake can be explained in part by the moon's gravitational focusing of its incident flow, a phenomenon considered in depth in Appendix D. These results are broadly morphologically consistent with the results for the density field and depositional pattern on Charon reported by Tucker et al. (2015).

The boundary condition at Charon's surface shapes flow in the near-Charon region. If particles are permitted to diffusely reflect from Charon, as opposed to permanently sticking on its frost regions, they may continue to 'hop' along its surface. Such particles may be considered as adsorbing to the surface, equilibrating to the local temperature, and being diffusely re-emitted in a process

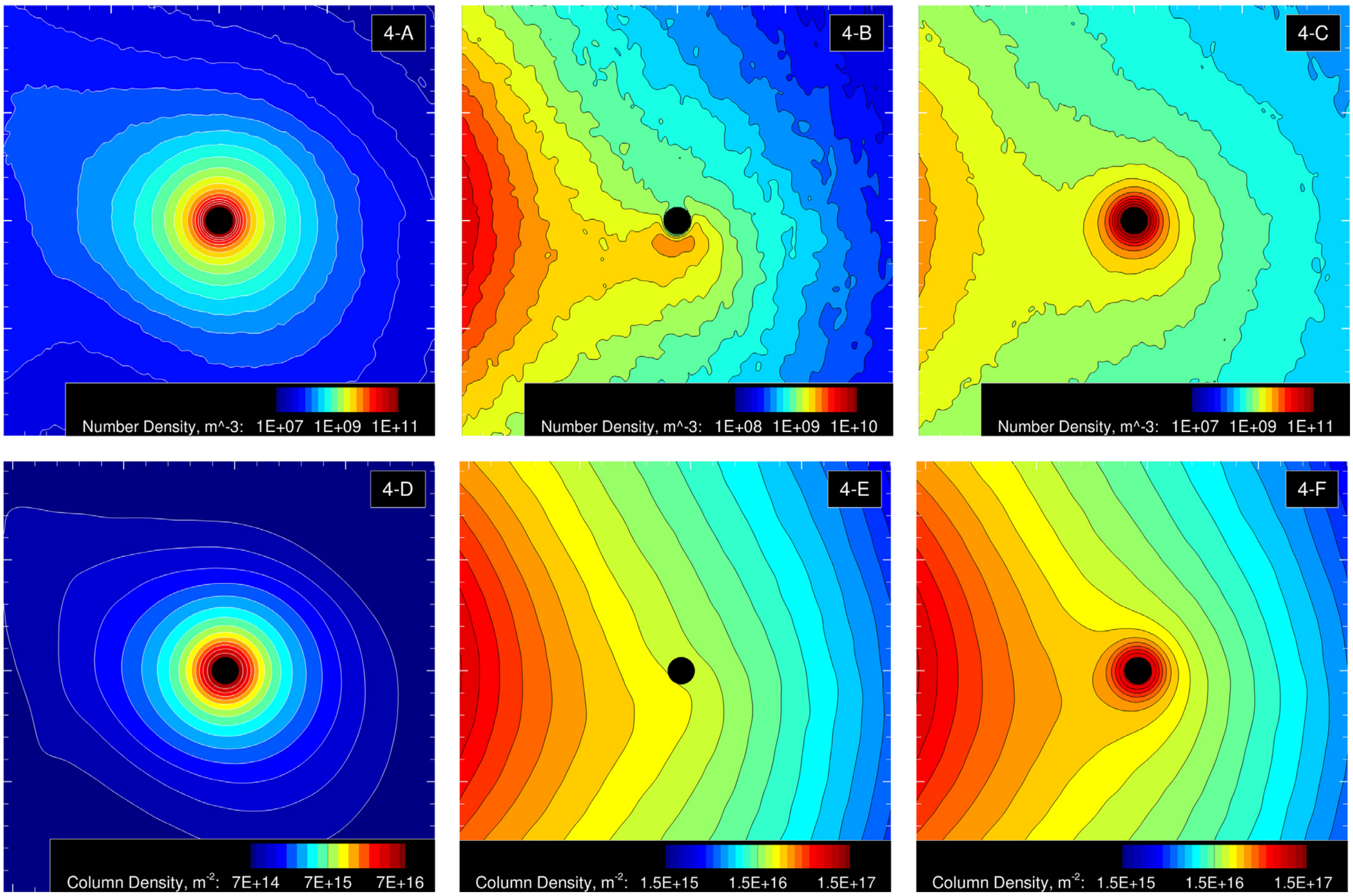

Fig. 4. The top panels (a–c) show number densities, while the bottom row (d–f) show column densities integrated along the polar axis. At left (a, d) are particles which have struck and reflected off Charon alone; at center (b, e) the result for the flowfield in which all particles stick to Charon; and at right (c, f) is the super-imposition: the total flowfield, permitting diffuse reflection.

that will ultimately result either in their escape or their travel to, and deposition in, a sufficiently cold region. While particles hop, they may have the effect of creating a persistent atmosphere about Charon. To escape, an emitted particle must have kinetic energy in excess of its gravitational potential at the surface, and will have been drawn from the tail of a Maxwellian distribution. In these steady-state calculations, the residence times of adsorbed particles are not relevant.

The simulation shown in Fig. 2 applies a uniform sticking condition at Charon. The Case A study is continued in a separate simulation, however, by re-emitting the particles stored at Charon as though they had diffusely reflected from its 53 K uniform surface. All further collisions with Charon are then treated in the same fashion so that particles tend to hop over Charon's surface. The resultant flow is sufficiently rarefied as to be non-collisional, and may be superposed with the result in which all particles stick to Charon, which is also non-collisional in the near-Charon region. The effect is that of two distinct flows and simulations, one of which contains all particles that *have* interacted with the surface (via diffuse reflection), and the other containing only particles that *have not* interacted with Charon's surface (i.e. that shown in Fig. 2, and equivalent to a uniform sticking condition: all particles in this field that have interacted with Charon have stuck). Summing these yields a result for a total flowfield that permits diffuse reflection at Charon. These flows are shown from left to right in Fig. 4, each panel of which occupies a square region 20,000 km on edge centered at Charon in the equatorial plane, as demonstrated by the dashed white region of Fig. 2. A diffuse transfer structure from Charon back toward Pluto is evident in the reflected particles, while the near-Charon region highlights the shape of the gas transfer structure arcing through the L1 point.

These two cases, in which either all particles stick at Charon or all particles reflect, bracket the range of possibilities for Charon's boundary conditions. If particles are permitted to bounce off of Charon, the Fig. 4 result suggests that a thin atmosphere could persist on the moon, an atmosphere effectively shared between bodies in a binary system. The maximum pressures of such an atmosphere in this Case A simulation are $O[10^{-15}]$ bar, significantly lower than would have been detectable by the NH instrumentation at $O[10^{-12}]$ bar.

Two radii above the Charon surface, roughly half of the local number density is composed of reflected particles, as shown in Fig. 5. Fig. 5 shows the same inset domain about Charon, 20,000 km on edge, as Fig. 4. This atmospheric feature shows an asymmetric effect about Charon along the axis perpendicular to the polar and Pluto–Charon axes: Charon's leading face sees, proportionally, more atmosphere perpetuated by surface interaction, corresponding to the inflated wakeward density and an isotropic distribution of particles leaving Charon's surface (after many diffuse reflections).

In examining flowfield structure, it is important to note that the flow above Pluto's exobase trends toward a free-molecular state in which individual particles only rarely experience collisional interactions. The DSMC results exhibit comparable structure to the Roche transfer phenomenon that occurs between semi-detached binary stars, as in the Algol system (Blondin et al., 1995) when one partner overfills its equipotential surface, demonstrated in

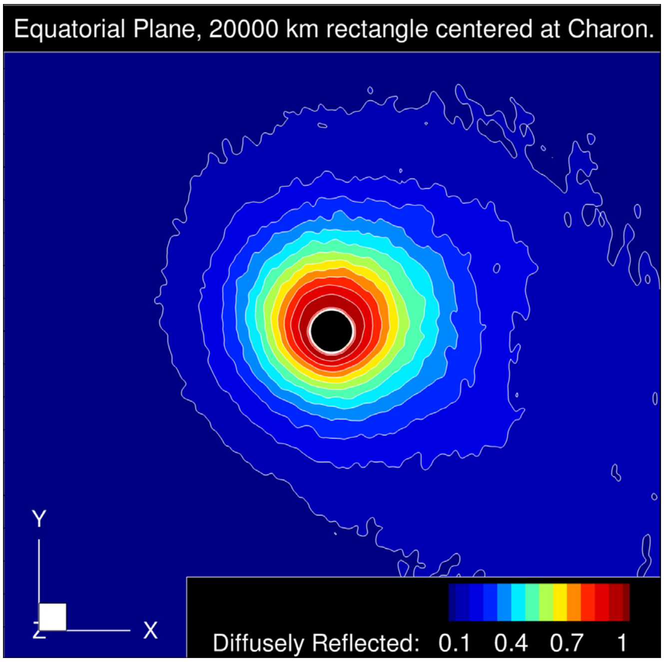

Fig. 5. The fraction of particles in the region about Charon that have reflected from its surface. The reflected particles perpetuate a thin atmosphere, with pressure under 10 femtobar. This superposed flowfield represents a result in which all particles that initially arrive at Charon reflect diffusely with temperatures equilibrated to the surface temperature (uniform at 53 K), accurate in the steady-state.

Table 3
The selected Case B lower boundary parameters, drawn from NH observation, and rates of vacuum escape and flux to Charon's surface.

Exobase conditions	Case B boundary	NH observation
Temperature T [K]	69	~ 70
Nitrogen n_{N2} [10^{12} m^{-3}]	5.5	4–7
Methane n_{CH4} [10^{12} m^{-3}]	4.0	3–5
Total number density n [10^{12} m^{-3}]	9.5	7–12
Exobase (boundary) altitude [km]	2800	2750–2850
System escape rate [s^{-1}]	7×10^{25} (>99% CH_4)	5 – 6×10^{25} (>99% CH_4)
Flux to Charon [s^{-1}]	2×10^{24} (~98% CH_4)	

Fig. 6. However, Roche theory is fundamentally hydrodynamic, its equations continuum in origin. The DSMC result is an ensemble and time average across a collection of particles primarily engaged in non-collisional and independent ballistic trajectories and not a representation of a 'bulk' flow; therefore, the structure of the Pluto–Charon density field, and specifically the nature of transfer to Charon, are distinct phenomena unique to a rarefied escaping atmosphere shared among bodies in a binary configuration.

4. Pluto–Charon at the New Horizons encounter

A second simulation, labeled Case B, is performed with boundary conditions from the New Horizons encounter for the atmosphere generated at the exobase conditions. As a result, the situation should directly match other NH observables, like vacuum escape rate. Case B is performed at an f_{num} of 5×10^{25} on 240 processors, and results shown were run to $\sim 10.5 \times 10^6$ s (19 diurnal cycles). The significant changes between Case B and the unheated pre-encounter exobase (Case A) are the exobase temperature and methane fraction: New Horizons observed a cold ~70 K exobase at ~42% methane, as detailed in Table 1. Vacuum escape rates and rates of deposition onto Charon are calculated for the equilibrated DSMC calculation and compared to those reported by Gladstone et al. (2016) and Bagenal et al. (2016), and the Case B simulation is shown to match the NH observed vacuum escape rate closely. Results and relevant boundary parameters are reported in Table 3.

Likewise, the structure of the Case B density field, its total rates of deposition and escape, and the depositional pattern observed on Charon do not change markedly from the Case A result. Fig. 7 shows the Case B flowfield both in a hemispheric region of 32,000 km radius and in a 20,000 km square about Charon for direct comparison against Figs. 2 and 4. The escape rate and total rate of flux to Charon for Case B are each about double the corresponding rates for Case A, which agrees with the ratio of total unperturbed Jeans escape rates at the two exobase conditions. The flowfields of Case B show the same transfer structures and Charon-wakeward asymmetries of Case A, as evidenced in Figs. 7–9.

The translational temperature of the highly-nonequilibrium flow about Charon is shown in the bottom left panel of Fig. 7. The velocity distribution of this flow is non-Maxwellian, and its tail is enhanced with high-speed particles. Note the enhancement in translational temperature as flow about Charon is gravitationally focused into the high-density region in the moon's wake. Additional discussion of this gravitational focusing effect is included in Appendix D.

Individual particles can be characterized by their mechanical (total) energy: the sum of their kinetic and (negatively-signed) gravitational potential energies in an inertial, barycentric reference frame. Particles with positive potential energies may escape, while particles with negative energies are, in a sense, gravitationally bound. The vast bulk of molecules fall into the latter category, having insufficient energies to escape the system, unsurprising as the

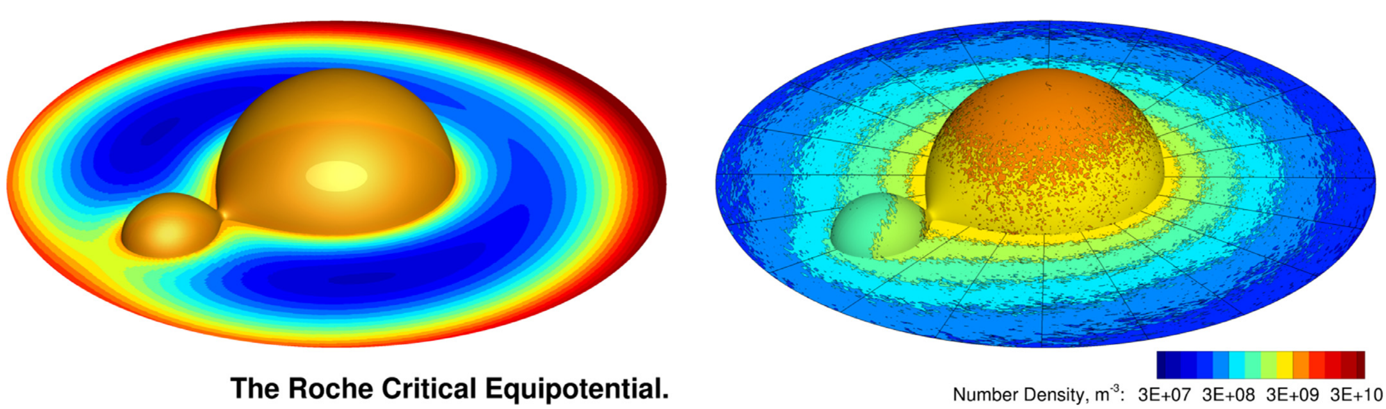

Fig. 6. (Left) The Roche equipotential surface connects the potential lobes about Pluto and Charon through the L1 Lagrange point and is the defining surface parameterizing gas transfer between semi-detached binary stars. While the potential is critical in considerations of particle mechanical energy (e.g. for propagating particles in satellite orbits, as in Beth et al., 2014), the theory governing Roche transfer is developed in fundamentally continuum terms. (Right) The number density field for Case A is projected onto the Roche equipotential surface.

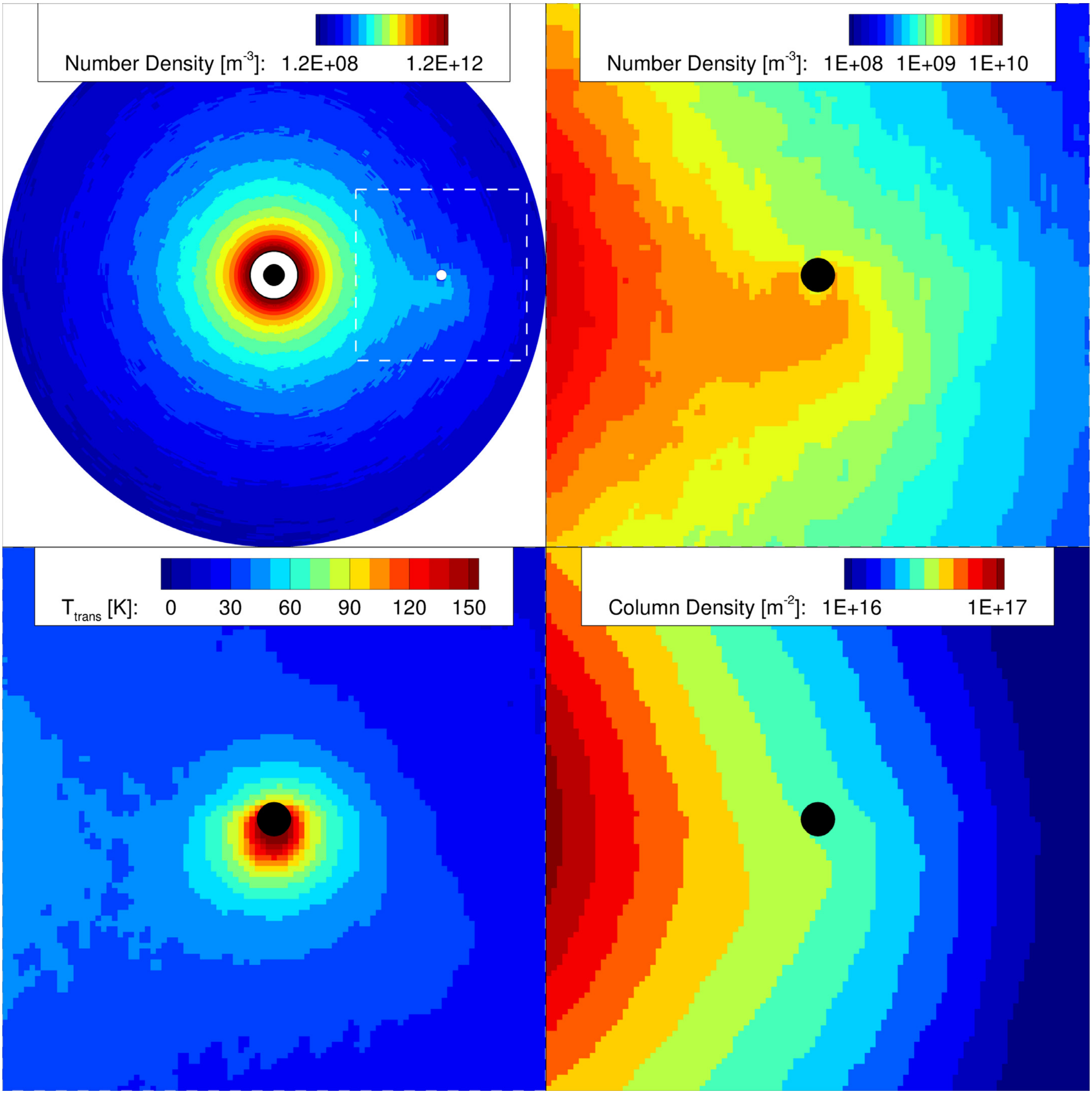

Fig. 7. (Top left) Number density about Charon in the NH simulation, Case B. The dashed square marks an inset region 20,000 km on edge about Charon, shown in the remaining panels. (Top right) The bridging gas transfer structure which arcs toward Charon's trailing hemisphere is preserved in Case B. (Bottom left) The translational temperature, a frame-independent result, peaks towards Charon's trailing hemisphere. (Bottom right) Column density LOS integrations down the polar axis demonstrate a slight wakeward asymmetry, but emphasize that the bridging structure is confined to a narrow, equatorial band when the boundary condition at Charon is uniform sticking.

mean thermal speed at the exobase is about one-third the escape velocity from Pluto. The Maxwellian draw of a high-energy particle is correspondingly rare, and the alternative routes for escape are either an imbuement of energy via collision, or an accelerating interaction with Charon (which itself requires substantial energy to reach). In Fig. 10, narrow bands of mechanical energies about zero are considered: these represent particles with potential and kinetic energies nearly equivalent. Such particles will approach the edge of the system and either narrowly escape to vacuum, or fall back into the domain over a long time-span. For this specific class of particles, a coherent spiral structure is visible with consistently-spaced bands trailing the wakeward hemispheres of Pluto and Charon; Pluto's band is more diffuse. This result suggests that the Pluto–Charon system may leave a detectable cork-screw tail, if only certain energy molecules were taken up by the solar wind.

5. Summary and conclusions

A fully three-dimensional model of the steady-state, rarefied component of Pluto's upper atmosphere is presented, demonstrated for the pre-encounter prediction most similar to that observed by New Horizons, and applied in a simulation of the NH

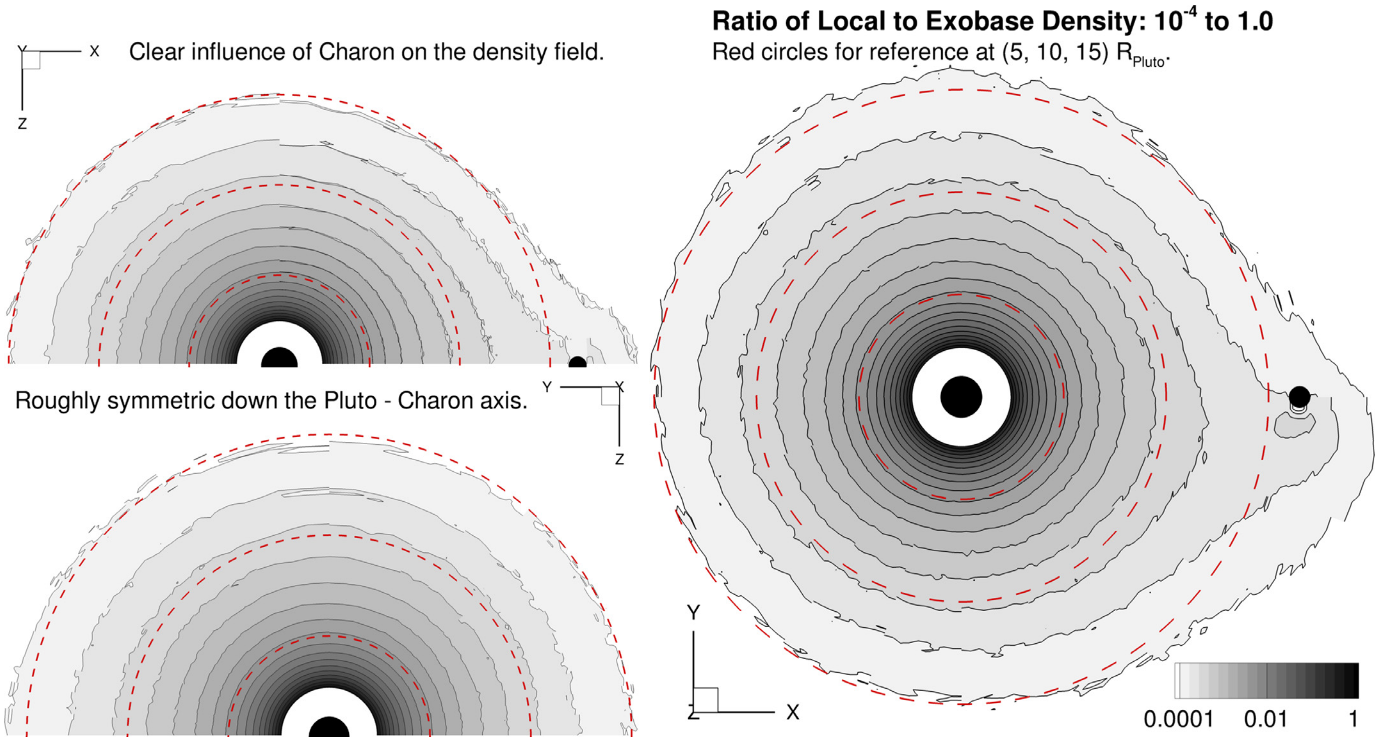

Fig. 8. In the Case B New Horizons result, number density decreases rapidly with radial distance from Pluto: for most of the flow the ratio of local to exobase density reaches 10^{-4} by 15 R_P. The region around Charon is an exception, as the density field is shown to distort toward the moon both along the Pluto–Charon axis and in its wake. This structure has comparable shape to that seen in the Case A field (Fig. 2).

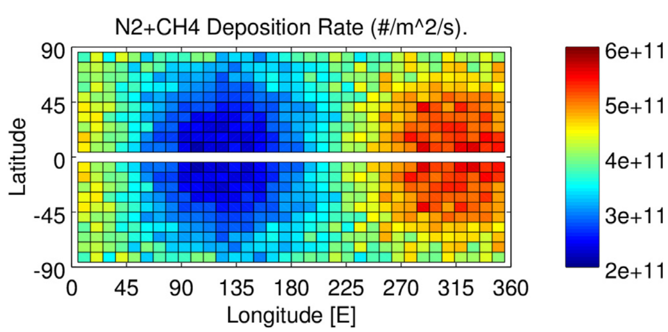

Fig. 9. In the New Horizons simulation (Case B), depositional rates onto Charon are comparable in magnitude and structure to those in the no-heat simulation (Case A), but methane now composes about 98% of the flux relative to nitrogen. This corresponds to the increase in exobase molar fraction from 0.44%, as hypothesized pre-encounter, to fully 42%: as a lighter species, methane preferentially escapes.

encounter exobase and resultant flowfield. While the majority of the domain by volume can be well approximated by free-molecular flow, we do find molecular collisions in the upper atmosphere (near the plutonian exobase) to be significant in shaping the flowfield, both by promoting flux from the plutonian exobase to Charon and by increasing the proportion of that flux generated on the exobase's anti-Charon hemisphere. Results for exobase parameters and rates of escape to vacuum and transfer to Charon are compared against the pre-encounter literature and against the observations of New Horizons, matching well with the latter.

Gas-transfer structures are noted in a binary atmospheric configuration, including preferential deposition of material from Pluto's escaping atmosphere onto Charon's leading hemisphere, peaking at 315° E (45° W) along the equator. As the moon gravitationally focuses incident flow a high density structure forms in its wake, discussed in Appendix D. In the event of total diffuse reflection from Charon, a returning flux forms that is preferentially directed toward Pluto's trailing hemisphere. Charon is shown to be capable of supporting a thin atmosphere at column densities as high as 1.5×10^{17} m^{-2} in simulations with a plutonian exobase condition similar to that observed by New Horizons and a diffusely reflective boundary at Charon's surface. Case B, computed from the observed NH exobase, yields a vacuum escape rate of 7×10^{25} CH_4 s^{-1} in good agreement with that encountered (Bagenal et al., 2016; Gladstone et al., 2016) and a rate of deposition onto Charon of 2×10^{24} s^{-1} of which ~98% is methane.

Improved boundary conditions for Charon anticipated in forthcoming New Horizons results include frost properties, fractional maps, and surface temperature distributions which will allow for refined simulations of the transport of 'hopping' particles along Charon's surface that inform the study of geologic features, like the dark red region at Mordor Macula formed when methane cold-trapped at Charon's poles is photolytically processed into tholins (Grundy et al. 2016). We have not considered the effects of UV radiation or solar wind charge exchange in these simulations; given Pluto's extreme distance from the sun, we anticipate low loss rates to photoprocesses. The NH results presented by Bagenal et al. (2016) suggest that upper atmospheric interactions with the solar wind do occur within our domain, but also that such interactions are unlikely to influence our solutions given the low reported densities of pick-up CH_4 (O[10^2 m^{-3}]) close to Pluto. Such phenomena may be addressed in future work. Improvements to existing plutonian GCMs would allow for the hybridization of our DSMC with fluid models at the continuum-rarefied boundary.

Acknowledgments

The research is supported by the NASA Outer Planets Research (OPR) grant NNX11AD88G. Computational resources were provided by the Texas Advanced Computing Center (TACC).

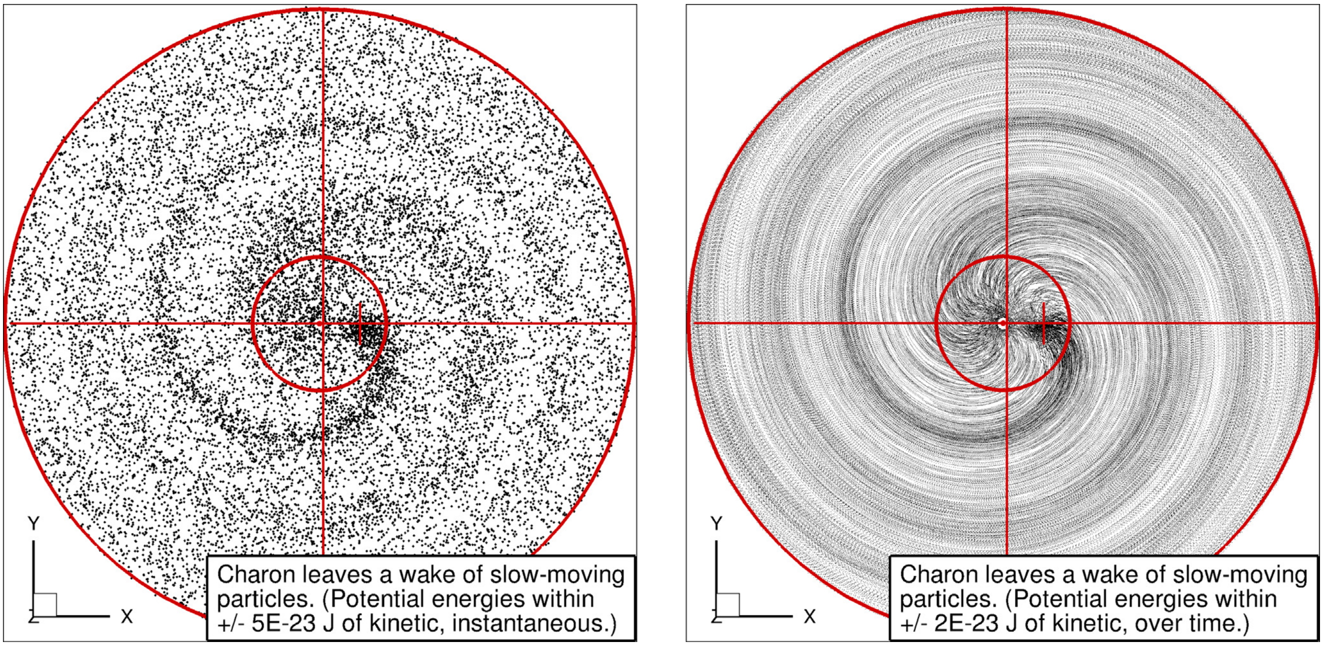

Fig. 10. (Left) An instantaneous depiction of a subset of computational particles with mechanical energies in the range $\pm 5 \times 10^{-23}$ J. The domain shown extends to 150,000 km from Pluto's center, while the interior circle shows a portion of the computational domain extending to 30,000 km consistent with that depicted in Figs. 2, 7, and 8. The axes cross on the barycenter, and Charon's position is marked with a cross. (Right) The trajectories of a narrower subset of these particles, $\pm 2 \times 10^{-23}$ J, are shown over a 20 h period to emphasize this spiral pattern.

Appendix A. Details on DSMC simulations

Table A.1 lists the relevant Pluto-Charon system parameters used in this work, in comparison to those reported by New Horizons and employed in the Tucker et al. (2015) simulations, while Table A.2 records relevant DSMC species parameters. Figure A.1 details the Pluto-Charon system geometry applied in our model.

Table A.1
Parameters of Pluto–Charon system used in DSMC simulations.

System parameters	New horizons	This work	Tucker et al. (2015)
Rotational period (d)	6.3872	6.3872	6.3657
Rotational period (s)	551,854	551,857	550,000
Radius, Pluto (km)	1187 ± 4	1185	1150
Radius, Charon (km)	606 ± 3	603.5	606
Mass, Pluto (10^{22} kg)	1.303 ± 0.003	1.304	1.3
Mass, Charon (10^{21} kg)	1.586 ± 0.015	1.519	1.5
Charon axis (km)	19,596	19,571	19,550

Table A.2
Species parameters used in DSMC simulations.

Species parameters	N_2	CH_4
Mass (kg)	4.652×10^{-26}	2.663×10^{-26}
Diameter (m)	3.580×10^{-10}	4.830×10^{-10}
Rotational DOF	2	3
Vibrational DOF	1	4
VHS Viscosity Exponent	0.68	0.84

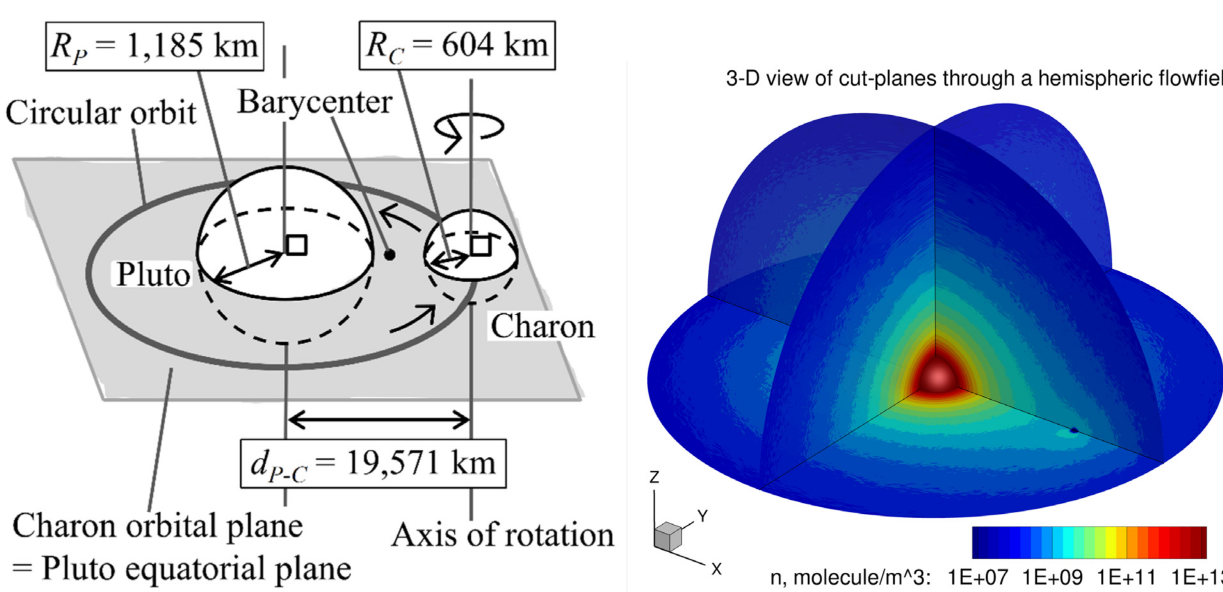

Fig. A.1. (Left) Schematic of Pluto–Charon system used in simulations. (Right) A 3-D representation of the computed flowfield, demonstrating system geometry and highlighting number densities about Charon.

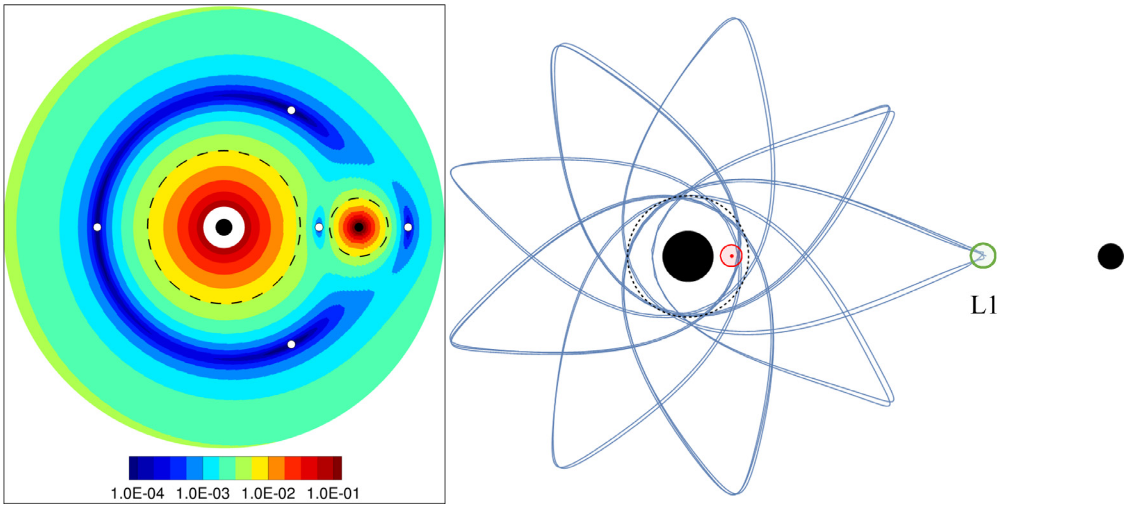

Fig. B.1. (Left) Schematic of the gradient of effective potential in the Pluto–Charon system, with Lagrange point coordinates indicated in white points, and Pluto and Charon in black. (Right) The trajectory of a test particle perturbed from L1 equilibrium, from initialization to 5×10^6 s. The system barycenter is marked in red, the L1 point in green, and the plutonian exobase in a black, dashed line. (For interpretation of the references to colour in this figure legend, the reader is referred to the web version of this article.)

Appendix B. A high-order scheme for particle trajectory integration

A consideration of integrator accuracy is motivated by steep gradients in effective potential around each of the Lagrange points as illustrated in Fig. B.1(a), and the long time scales of settling (O[10^6] s) in system fluxes compared to the most limiting collision timescales (O[10^2] s). A simple but restrictive study may be performed by placing test particles at the five Lagrange points of the system, all of which are unstable for the Pluto–Charon case, and determining the time it takes the particles to start moving away from these positions. For such a case we find that, for the 2nd-order scheme, it takes O[10^5] s for all five test particles to depart their equilibrium positions. By comparison, for the higher-order RKPD scheme we employ in the DSMC simulations, only after 10^6 s are the L1 and L2 particles perturbed from their equilibrium Lagrange positions, while after 5×10^6 s the L4 and L5 test particles remain unmoved. A representative trajectory of an L1 test particle is indicated in Fig. B.1(b). Since transfer from Pluto to Charon occurs roughly along their axis and through L1, we were therefore motivated to use the RKPD higher-order scheme to ensure accuracy in this critical region. This higher-order and adaptively time-stepped integrator also allowed us to use time-steps limited by the mean time between collisions at the exobase (~200 s) instead of the O[1 s] time-steps used in applying the RK2 scheme in our prior work. An additional motivating factor was our observation of the existence of a class of particles that remain in flight over many millions of seconds: even if such particles are unlikely to occupy satellite orbits given Charon's perturbative effect, integrating their trajectories accurately was a priority.

Appendix C. Simulations of the Tucker et al. (2015) heating cases

The exobase boundary conditions reported in Tucker et al. (2015) for a series of solar heating conditions are employed in that work in free-molecular simulations of an escaping flow of nitrogen at the medium solar heating condition. In this Appendix, 3-D DSMC simulations of each heating case are presented for an f_{num} of 10^{26} and for a molecular sticking condition at Charon's surface. While the exobase values from Tucker et al. (2015) overestimate the extent, escape rates, and nitrogen fraction of the observed plutonian atmosphere at the time of the New Horizons encounter, Gladstone et al. (2016) hypothesize that past nitrogen escape rates must have occasionally been much greater in order to explain the primarily erosional features on Pluto's surface. These DSMC simulations of transfer and escape for a variety of solar heating values and corresponding levels of exobase expanse are thus potentially illustrative of Pluto and Charon's past atmospheres. Table C.1 indicates the lower boundary conditions employed in these DSMC simulations, while Table C.2 reports the results for the fluxes into and out of the system for each case. The Tucker et al. (2015) case for medium solar heating is included for comparison. Our DSMC simulations are fully kinetic, representing collisions and physics absent from Tucker's free-molecular calculation, and are about two orders of magnitude better-resolved in particle count (related to f_{num}).

The high resolution of the present calculations allows for the three-dimensional visualization of their flowfields (Figs. C.1 and C.2), which demonstrate the archetypal features of a bridging

Table C.1
Exobase conditions reported in Tucker et al. (2015) employed as lower boundary conditions in the minimum, medium, and maximum solar heating cases addressed in Appendix C.

Exobase conditions	Minimum	Medium	Maximum
Exobase radius (R_P)	5.3	6.84	9.8
Temperature T (K)	87	79	66
Jeans parameter λ_x	5.7	4.8	4.5
Number density (10^{11} m^{-3})	7.0	5.0	3.0

Table C.2
Results for DSMC simulations at the various solar heating cases and exobase parameters.

Solar heating case	Maximum	Minimum	Medium (DSMC)	Medium (Tucker)
f_{num}	10^{26}	10^{26}	10^{26}	$<10^{28}$
Flux into domain (10^{28}/s)	2.8	2.2	2.5	2.5
Return flux into exobase (10^{28}/s)	2.2	2.1	2.3	>2.0
System escape (10^{27}/s)	5.8	1.1	2.2	2.2
Flux to Charon (10^{26}/s)	2.1	0.36	0.80	0.57
Ratio of Charon flux to System escape (%)	3.6	3.3	3.6	2.6

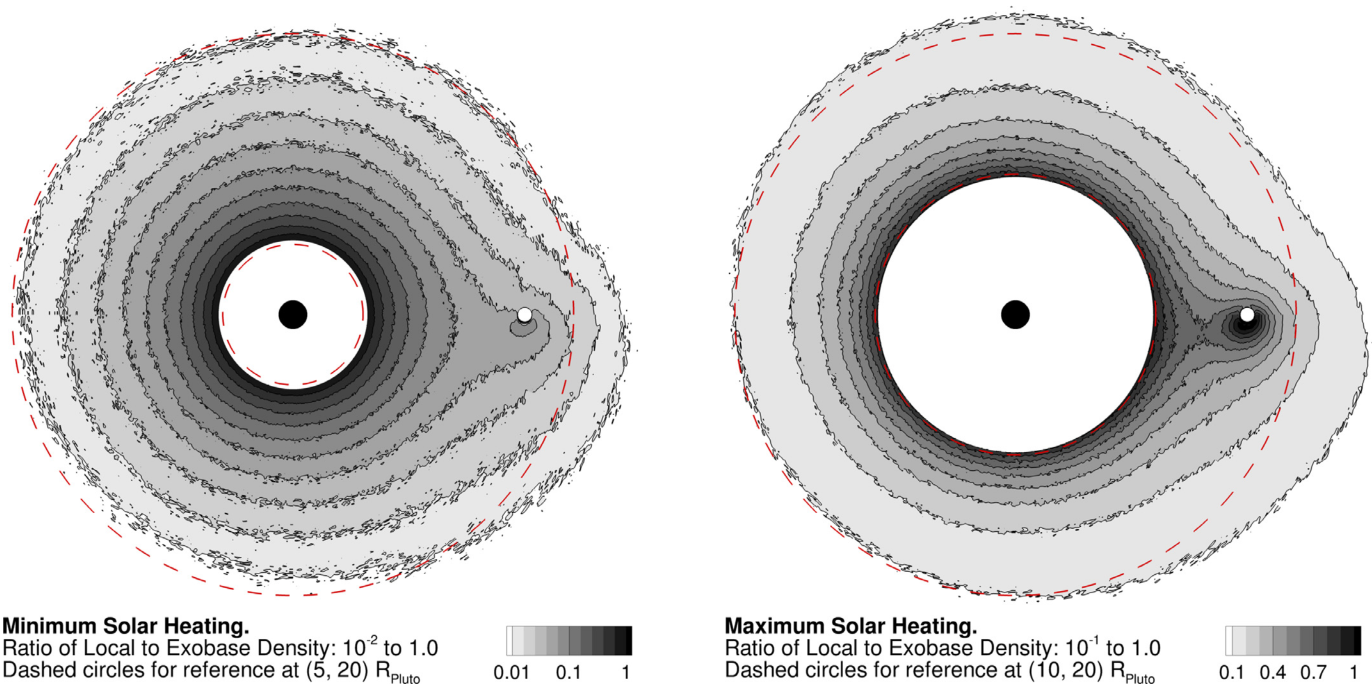

Fig. C.1. Ratios of local to exobase number density through the flowfield for steady-state solutions of the minimum and maximum heat cases from Tucker et al. (2015). The outer dashed circle for each system is drawn at 20 R_P and corresponds to a factor of $O[10^2]$ decrease in number density for the relatively compact minimum-heat escaping atmosphere, versus a factor of $O[10^1]$ depletion for the expansive maximum-heat case.

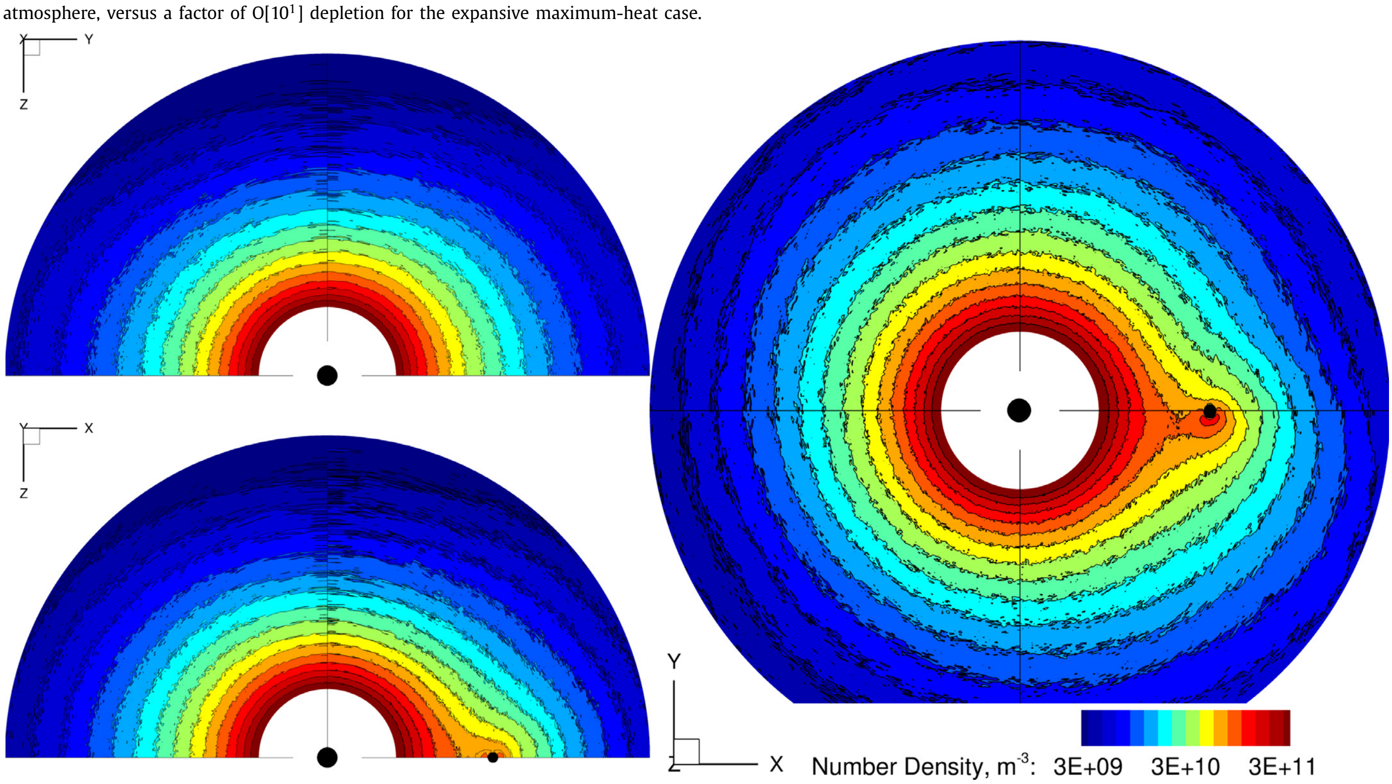

Fig. C.2. A steady-state 3-D flowfield computed for the medium heating case (Tucker et al. 2015), which shows comparable structure to the Case A and B results (compare to Figs. 2 and 7).

structure arcing wakeward through the L1 point, preferential deposition onto Charon's leading hemisphere, and an asymmetric distortion of the number density field behind Charon also visible in Cases A and B. It is notable that in the maximum-heat case, with the exobase extended fully 9.8 R_P and nearly to the L1 point, Charon retains an atmosphere of order exobase density, even as all particles incident on its surface stick.

Appendix D. The Bondi–Hoyle–Lyttleton accretion problem

An interesting result that emerges from simulations of rarefied gas dynamic transfer in the plutonian system is the apparent contradiction between the peak depositional flux from Pluto oriented onto Charon's leading hemisphere, opposite the occurrence of the peak flowfield density in Charon's wake. In explaining this phenomenon, an analogy can be made between Charon travelling

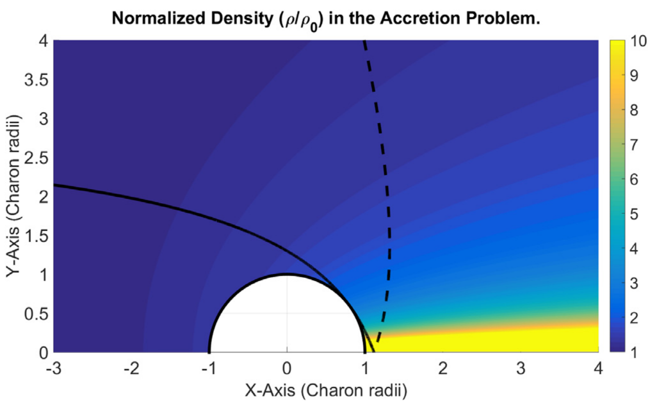

Fig. D.1. Contours of normalized density calculated for the analytic solution to the BHL accretion problem applied to Charon. All material between the (solid) critical trajectory and the axis will be incident onto Charon's face, while all other material will, in the accretion problem, be drawn through the symmetry axis in Charon's wake. If we consider that Charon impedes trajectories with initial impact parameters less than ζ_{CR}, the analytic density solution to the BHL problem is invalid between solid and dashed trajectories.

through Pluto's escaping atmosphere and a point mass traveling on a linear path through an infinite, uniform-density gas cloud.

The Bondi-Hoyle-Lyttleton accretion problem considers the gravitational focusing of such a cloud in the wake of a rapidly-travelling star and can be stated as an axisymmetric problem in cylindrical coordinates, with ζ an impact parameter representing distance normal to the symmetry axis infinitely far from the star, and v_∞ a freestream velocity oriented along that axis. Edgar (2004) presents a useful derivation of BHL theory in a polar coordinate system with its center at the point mass, followed here. The equations of motion and conservation of angular momentum for this system are:

$$\ddot{r} - r\dot{\theta}^2 = -\frac{GM}{r^2} \tag{D1}$$

$$r^2\dot{\theta} = \zeta v_\infty \tag{D2}$$

With a substitution of variables and application of the axisymmetric, steady-state continuity equation, analytic solutions for the radial coordinate r and flowfield density ρ are derived as functions of θ and ζ.

$$r = \frac{\zeta^2 {v_\infty}^2}{GM(1+\cos\theta) - \zeta {v_\infty}^2 \sin\theta} \tag{D3}$$

$$\rho = \frac{\rho_0\ \zeta^2}{r\sin\theta\,(2\zeta - r\sin\theta)} \tag{D4}$$

For gas in the infinite cloud, the velocity (v_∞) of the mass effectively acts as a hyperbolic excess velocity, as expressed in Eq. D5. Solving for velocity components and setting the radial component to zero at Charon's radius, R, allows for an expression of the impact parameters of the critical family of hyperbolae which will pass just tangent to the surface of Charon.

$$v^2 = {v_\infty}^2 + \frac{2\ GM}{r} = {v_r}^2 + {v_\theta}^2 \tag{D5}$$

$$\frac{\zeta_{CR}}{R} = \sqrt{1 + \frac{2\ GM}{R\ {v_\infty}^2}} \tag{D6}$$

Given a point of Charon's mass traveling through an infinite and uniform cloud of density ρ_0 in a straight line at Charon's angular velocity of ∼199.4 m/s, Figure D.1. represents the analytic solution to the cloud's normalized density. The critical, surface-tangent hyperbolae in this case have impact parameters of $\zeta_{CR} = 3.102\,R$, and are drawn in black (the dashed trajectory is the continuation of the solid trajectory across the symmetry axis). All material ahead of the point mass and within ζ_{CR} will be drawn into Charon's leading hemisphere, and all remaining material will be focused into Charon's wake. The distance behind Charon's center at which the convergence of these tangent trajectories occurs can be expressed:

$$\frac{D_{CR}}{R} = 1 + \frac{R\ {v_\infty}^2}{2\ GM} \tag{D7}$$

For Charon's parameters, this convergence occurs 0.1160 R behind Charon's trailing hemisphere. If Charon were to be considered as a body with radius R capable of impeding the flow, instead of a point, no trajectories would pass through the region between this convergence and Charon for the BHL problem.

The BHL analysis demonstrates how gravitational focusing draws material into Charon's leading hemisphere while increasing density in its wake as Charon travels through Pluto's escaping atmosphere. There are a number of simplifications that cause departure from this result in the DSMC simulations. Charon travels on a nearly circular orbit about the system barycenter, not in a straight line, and Pluto exerts a perturbing gravitational influence on the flow about its moon. Furthermore, Charon travels through a non-uniform gas cloud with a complex and non-equilibrium velocity distribution. These effects deflect the focused density in Charon's wake from the BHL problem's symmetry axis and shift the location of peak deposition onto Charon from the moon's leading face towards its sub-Pluto face, as evident in Figs. 2 and 3, respectively. The wide distribution of particle velocities and trajectories in the escaping plutonian flow also produces trajectories that are incident onto Charon's trailing hemisphere, where the BHL problem suggests no deposition will occur.

In addition to its utility as a simple model for the gravitational focusing process, the BHL analysis can be useful in explaining the 'hollow' regions in the density field that form behind Charon and ahead of the density convergence (particularly evident in the top-right panel of Fig. 7) and in estimating the total flux onto Charon's surface given the average flowfield density at Charon's distance.

Consider the critical convergence distance for the Charon system derived in Eq. D7. The BHL analysis for a spherical mass predicts that the region bounded by the moon and these hyperbolae form a wakeward region of zero density that extends to, given Charon's parameters, 0.1160 R. While the nonequilibrium and rarefied nature of the flow at Charon's distance from Pluto ensures that some class of particles will have trajectories that do carry them through this 'shadow region,' the BHL prediction aligns with presence and extent of the small pockets of low density visible between Charon and the high-density wake region evident in Fig. 4(b) and the top-right panel of Fig. 7.

Table D.1
Comparison of BHL model for flux to Charon vs. full 3-D calculations.

Parameters	Case A DSMC	Case B DSMC	Med. Heat DSMC	Med. Heat (Tucker)
n_∞ at Charon (10^9 m^{-3})	∼5	∼0.8	∼30	∼23
Flux to Charon, BHL (10^{24}/s)	∼11	∼1.8	∼66	∼51
Flux to Charon, 3-D model (10^{24}/s)	14–15	2.0	80	57

Likewise, an accurate analytic estimate of the total flux to Charon can be made given only a density result at Charon's distance from Pluto in a 1-D simulation. As all particles within the BHL problem's critical hyperbolae will be incident onto the sphere's face, this net number flux can be expressed

$$\zeta_{CR}^2\left(\pi R^2 v_\infty\right) n_\infty, \tag{D8}$$

which, for Charon's parameters, reduces to $2.195 \times 10^{15}\ n_\infty\ \mathrm{s}^{-1}$ for a number density in #/m^3. Estimates from this simple model are compared to the results of the Tucker et al. (2015) and our DSMC simulations of fully three-dimensional flowfields in Table D.1., given only n_∞ as the number density at Charon's distance, roughly estimated by the flowfield-averaged (or 1-D if available) density at Charon's distance.

References

Bagenal, F., et al., 2016. Pluto's interaction with its space environment: solar wind, energetic particles, and dust. *Science* 351, 8 aad9045.

Beth, A., Garnier, P., Toublanc, D., Dandouras, I., Mazelle, C., Kotova, A., 2014. Modeling the satellite particle population in planetary exospheres: application to Earth, Titan, and Mars. *Icarus* 227, 21–36.

Bird, G.A., 1994. Molecular Gas Dynamics and the Direct Simulation of Gas Flows. Oxford Univ. Press, New York.

Borgnakke, C., Larsen, P.S., 1975. Statistical collision model for Monte Carlo simulation of polyatomic gas mixture. J. Comp. Phys. 18, 405–420.

Blondin, J.M., Richards, M.T., Malinowski, M.L., 1995. Hydrodynamic simulations of the mass transfer in Algol. *Astrophys. J.* 445, 939–946.

Edgar, R., 2004. A review of Bondi–Hoyle–Lyttleton accretion. *New Astron. Rev.* 48, 843–859.

Elliot, J.L., et al., 2007. Changes in Pluto's atmosphere: 1988–2006. Astron. J. 134, 1–13.

Elliot, J.L., Dunham, E.W., Bosh, A.S., Slivan, S.M., Young, L.A., Wasserman, L.H., Millis, R.L., 1989. Pluto's atmosphere. *Icarus* 77, 148–170.

Erwin, J., Tucker, O.J., Johnson, R.E., 2013. Hybrid fluid/kinetic modeling of Pluto's escaping atmosphere. Icarus 226, 375–384.

Gladstone, G.R., Stern, S.A., et al., 2016. The atmosphere of Pluto as observed by new horizons. *Science* 351, 6 aad8866.

Grundy, W.M., Olkin, C.B., Young, L.A., Holler, B.J., 2014. Near-infrared spectral monitoring of Pluto's ices II: recent decline of CO and N_2 ice absorptions. *Icarus* 235, 220–224.

Grundy, W.M., et al., 2016. The formation of Charon's red poles from seasonally cold-trapped volatiles. *Nature* 19340, 4.

Hubbard, W.B., Hunten, D.M., Dieters, S.W., Hill, K.M., Watson, R.D., 1988. Occultation evidence for an atmosphere on Pluto. *Nature* 336, 452–454.

Hubbard, W.B., Yelle, R.V., Lunine, J.I., 1990. Nonisothermal Pluto atmosphere models. *Icarus* 84, 1–11.

Hunten, D.M., Watson, A.J., 1982. Stability of Pluto's atmosphere. *Icarus* 51, 665–667.

Ingersoll, A.P., 1990. Dynamics of Triton's atmosphere. *Nature* 344, 315–317.

Krasnopolsky, V.A., 1999. Hydrodynamic flow of N_2 from Pluto. J. Geophys. Res. 104, 5955–5962.

Lellouch, E., de Bergh, C., Sicardy, A., Forget, F., Vangvichith, M., Käufl, H.-U., 2015. Exploring the spatial, temporal, and vertical distribution of methane in Pluto's atmosphere. *Icarus* 246, 268–278.

McDoniel, W.J., Goldstein, D.B., Varghese, P.L., Trafton, L.M., 2015. Three-dimensional simulation of gas and dust in io's pele plume. *Icarus* 257, 251–274.

McNutt Jr., R.L., 1989. Models of Pluto's upper atmosphere. Geophys. Res. Lett. 16, 1225–1228.

Millis, R.L., Wasserman, L.H., Franz, O.G., Nye, R.A., Elliot, J.L., Dunham, E.W., Bosh, A.S., Young, L.A., Slivan, S.M., Gilmore, A.C., 1993. Pluto's radius and atmosphere: results from the entire 9 June 1988 occultation data set. *Icarus* 105, 282–297.

Moore, C.H., Goldstein, D.B., Varghese, P.L., Trafton, L.M., Stewart, B., 2009. 1-D DSMC simulation of Io's atmospheric collapse and reformation during and after eclipse. *Icarus* 201, 585–597.

Morris, A.B., Goldstein, D.B., Varghese, P.L., Trafton, L.M., 2015. Approach for modeling rocket plume impingement and dust dispersal on the moon. *J. Spacecraft Rockets* 52, 362–374.

Nanbu, K., 1986. Theoretical basis of the direct simulation Monte Carlo method. In: Rarefied Gas Dynamics: 15th International Symposium Proceedings 1. Teubner , Stuttgart, pp. 369–383.

Olkin, C., Young, E., Young, L., Grundy, W., Schmitt, B., Tokunaga, A., Owen, T., Roush, T., Terada, H., 2007. Pluto's spectrum from 1.0 to 4.2 μm: implications for surface properties. Astr. J. 133, 420–431.

Olkin, C., et al., 2014. Pluto's atmospheric structure from the July 2007 stellar occultation. *Icarus* 239, 15–22.

Olkin, C., et al., 2015. Evidence that Pluto's atmosphere does not collapse from occultations including the 2013 May 04 event. *Icarus* 246, 220–225 .

Owen, T.C., Roush, T.L., Cruikshank, D.P., Elliot, J.L., Young, L.A., de Bergh, C., Schmitt, B., Geballe, T.R., Brown, R.H., Bartholomew, M.J, 1993. Surface ices and the atmospheric composition of Pluto. *Science* 261, 745–748.

Pasachoff, J.M., Souza, S.P., Babcock, B.A., Ticehurst, D.R., Elliot, J.L., Person, M.J., Clancy, K.B., Roberts Jr., L.C., Hall, D.T., Tholen, D.J., 2005. The structure of Pluto's atmosphere from the 2002 August 21 stellar occultation. Astron. J. 129, 1718–1723.

Person, M.J., et al., 2008. Waves in Pluto's upper atmosphere. Astron. J. 136, 1510–1518.

Protopapa, S., Boehnhard, H., Herbst, T.M., Cruikshank, D.P., Grundy, W.M., Merlin, F., Olkin, C.B., 2008. Surface characterization of Pluto and Charon by L and M band spectra. *Astron. Astrophys.* 490, 365–375.

Prem, P., Artemieva, N.A., Goldstein, D.B., Varghese, P.L., Trafton, L.M., 2015. Transport of water in a transient impact-generated lunar atmosphere. *Icarus* 255, 148–158.

Sicardy, B., Widemann, T., Lellouch, E., Veillet, C., Cuillandre, J.-C., Colas, F., Roques, F., Beisker, W., Kretlow, M., Lagrange, A.-M., Gendron, E., Lacombe, F., Lecacheux, J., Birnbaum, C., Fienga, A., Leyrat, C., Maury, A., Raynaud, E., Renner, S., Schultheis, M., Brooks, K., Delsanti, A., Hainaut, O.R., Gilmozzi, R., Lidman, C., Spyromilio, J., Rapaport, M., Rosenzweig, P., Naranjo, O., Porras, L., Diaz, F., Calderon, H., Carillo, S., Carvajal, A., Recalde, E., Gaviria Cavero, L., Montalvo, C., Barria, D., Campos, R., Duffard, R., Levato, H., 2003. Large changes in Pluto's atmosphere as revealed by recent stellar occultations. *Nature* 424, 168–170.

Spencer, J.R., Stansberry, J.A., Trafton, L.M., Young, E.F., Binzel, R.P., Croft, S.K., 1997. Volatile transport, seasonal cycles, and atmospheric dynamics on Pluto. In: Stern, S.A., Tholen, D.J. (Eds.), Pluto and Charon. University of Arizona Press, Tucson, pp. 435–473.

Stern, S.A., 1981. Theoretical investigations of the atmospheric environment of pPluto. Thesis, University of Texas, Austin. 232 pp.

Stern, S.A., et al., 2015. The Pluto system: initial results from its exploration by new horizons. *Science* 350, 8 aad1815.

Stern, S.A., et al., 2016. New Horizons constraints on Charon's present day atmosphere. *Icarus* https://arxiv.org/abs/1608.06955.

Stewart, B.D., Pierazzo, E., Goldstein, D.B., Varghese, P.L., Trafton, L.M., 2011. Simulations of a comet impact on the Moon and associated ice deposition in polar cold traps. *Icarus* 215, 1–16.

Strobel, D.F., 2008. N_2 escape rates from Pluto's atmosphere. *Icarus* 193, 612–619.

Tian, F., Toon, O., 2005. Hydrodynamic escape of nitrogen from Pluto. Geophys. Res. Lett. 32, L18201.

Trafton, L.M., 1990. A two-component volatile atmosphere for Pluto. 1. The bulk hydrodynamic escape regime. Astrophys. J. 359, 521–523.

Trafton, L.M., Hunten, D.M., Zahnle, K.J., McNutt Jr., R.L., 1997. Escape processes at Pluto and Charon. In: Stern, S.A., Tholen, D.J. (Eds.), Pluto and Charon. University of Arizona Press, Tucson, pp. 475–522.

Trafton, L.M., Stern, S.A., 1983. On the global distribution of Pluto's atmosphere. Astrophys. J. 267, 872–881.

Tucker, O.J., Erwin, J.T., Deighan, J.I., Volkov, A.N., Johnson, R.E., 2012. Thermally driven escape from Pluto's atmosphere: a combined fluid/kinetic model. *Icarus* 217, 408–415.

Tucker, O.J., Johnson, R.E., Young, L.A., 2015. Gas transfer in the Pluto–Charon system: a Charon atmosphere. *Icarus* 246, 291–297.

Volkov, A.N., Johnson, R.E., Tucker, O.J., Erwin, J.T., 2011. Thermally driven atmospheric escape: transition from hydrodynamic to Jeans escape. Astrophys. J. Lett. 729 (L24), 5.

Wagner, W., 1992. A convergence proof for Bird's direct simulation Monte Carlo method for the Boltzmann equation. J. Stat. Phys. 66, 1011–1044.

Walker, A.C., Gratiy, S.L., Goldstein, D.B., Moore, C.H., Varghese, P.L., Trafton, L.M., Levin, D.A., Steward, B., 2010. A comprehensive numerical simulation of Io's sublimation-driven atmosphere. *Icarus* 207, 409–432.

Walker, A.C., Moore, C.H., Goldstein, D.B., Varghese, P.L., Trafton, L.M., 2012. A parametric study of Io's thermophysical surface properties and subsequent numerical atmospheric simulations based on the best fit parameters. *Icarus* 220, 225–253.

Yelle, R.V., Elliot, J.L., 1997. Atmospheric structure and composition: Pluto and Charon. In: Stern, S.A., Tholen, D.J. (Eds.), Pluto and Charon. University of Arizona Press, Tucson, pp. 347–390.

Yeoh, S.K., Chapman, T.A., Goldstein, D.B., Varghese, P.L., Trafton, L.M., 2015. On understanding the physics of the Enceladus south polar plume via numerical simulation. *Icarus* 253, 205–222.

Young, E.F., et al., 2008. Vertical structure in Pluto's atmosphere from the 2006 June 12 stellar occultation. Astron. J. 136, 1757–1769.

Young, L.A., Elliot, J.L., Tokunaga, A., de Bergh, C., Owen, T., 1997. Detection of gaseous methane on Pluto. *Icarus* 127, 258–270.

Zalucha, A.M., Gulbis, A.A.S., Zhu, X., Strobel, D.F., Elliot, J.L., 2011. An analysis of Pluto occultation light curves using an atmospheric radiative-conductive model. *Icarus* 211, 804–818.

Zhang, J., Goldstein, D.B., Varghese, P.L., Gimelshein, N.E., Gimelshein, S.F., Levin, D.A., 2003. Simulation of gas dynamics and radiation in volcanic plumes on Io. *Icarus* 163, 182–197.

Zhang, J., Goldstein, D.B., Varghese, P.L., Trafton, L.M., Moore, C., Miki, K., 2004. Numerical modeling of Ionian volcanic plumes with entrained particulates. *Icarus* 172, 479–502.